The mixing region in freely decaying variable-density turbulence

Pooya Movahed[1],† and Eric Johnsen[1]

[1]Department of Mechanical Engineering, University of Michigan, Ann Arbor, MI 48109, USA

A novel set-up is proposed to numerically study turbulent multimaterial mixing, starting from an unperturbed material interface between a light and a heavy fluid. We conduct direct numerical simulation (DNS) to better understand the role of density gradient alone on the turbulence, specifically with regard to the mixing region dynamics and anisotropy across scales. Freely decaying isotropic turbulent fields of different densities but identical kinematic viscosities are juxtaposed. The rationale for this strategy is that conventional turbulence scalings are based on kinetic energy per unit mass and kinematic viscosity. Thus, by matching the initial kinematics (root-mean-square velocity) and the dissipation (kinematic viscosity), the turbulence (kinetic energy per unit mass) decays at the same rate in both fluids. With this set-up, the effect of the density gradient alone on the turbulence can be considered, independently from other contributions (e.g. mismatch in kinetic energy per unit mass, acceleration field, etc.). We examine the mixing region dynamics at large and small scales for different density ratios and Reynolds numbers. After an initial transient, we observe a self-similar growth of the mixing region, which we explain via theoretical arguments verified by the DNS results. Inside the mixing region, the momentum of the heavier eddies causes the mean interface location to shift toward the light fluid. A higher density ratio leads to a wider, less molecularly mixed mixing region. Although anisotropy is evident at the large scales, the dissipation scales remain essentially isotropic, even at the highest density ratio under consideration (12:1). The intermittency of the velocity field exhibits isotropy, while the mass fraction field is more intermittent in the direction of the density gradient.

Key words: intermittency, isotropic turbulence, turbulent mixing

1. Introduction

Turbulence effectively mixes fluids through a multiscale process (Danckwerts 1952, 1958; Dimotakis 2005): fluids are entrained at the largest scales, dispersed by eddies of varying sizes until the length and time scales are sufficiently small for viscous, heat and mass diffusion to act. Dimotakis (2005) suggests that turbulent mixing can be categorized into three 'levels'. Extensive research has been dedicated to understanding mixing of passive scalars (level 1), which is decoupled from the fluid dynamics (Warhaft 2000; Sawford 2001), specifically in the context of dispersion

† Email address for correspondence: pooyam@umich.edu

of collections of small particles in turbulent flows, e.g. pollutants, smoke or, under certain circumstances, clouds. At the other end of the spectrum, level 3 mixing is characterised by a strong coupling between the fluid dynamics and the composition of the fluids, such as in combustion processes. A variety of problems in atmospheric, oceanic and astrophysical flows lie in between, where the mixing is coupled to the dynamics (level 2 mixing), e.g. through variations in density and composition, but with little modification to the fluids themselves. A considerable amount of research in level 2 mixing, the focus of this work, is concerned with hydrodynamic instabilities at interfaces (Chandrasekhar 1961; Sharp 1984; Rogers & Moser 1992; Brouillette 2002) driven by continuous and impulsive acceleration fields (Rayleigh–Taylor and Richtmyer–Meshkov) and shear (Kelvin–Helmholtz), which may ultimately evolve to turbulence. At the present time, there is no consensus as to whether the resulting turbulence can be described by Kolmogorov–Obukhov ideas (Soulard & Griffond 2012) or not (Poujade 2006; Abarzhi 2010). The lack of understanding of turbulent mixing has impeded progress in a variety of problems, e.g. understanding how heavy and light elements mix after the collapse of a supernova (Kifonidis *et al.* 2006) and the inability to achieve ignition in inertial confinement fusion (Lindl 1995; Thomas & Kares 2012).

One of the main difficulties in level 2 mixing lies in the realisation that the turbulence is not isotropic at all scales, thus preventing direct application of classical Kolmogorov–Obukhov–Corrsin (KOC) theory (Kolmogorov 1941; Obukhov 1949; Corrsin 1951). From a pragmatic viewpoint, the Rayleigh–Taylor instability is a useful illustration of anisotropy in turbulence (Cabot & Cook 2006; Abarzhi 2010). Large-scale features such as density variations and an acceleration field (e.g. body force, rotation) introduce an asymmetry, thus leading to anisotropy. The misalignment of the (hydrostatic) pressure and density gradients at unstably stratified interfaces generates baroclinic vorticity that feeds the instability, thus ultimately leading to fully mixed turbulence through a multistage process (Cook & Dimotakis 2001; Cabot & Cook 2006). Anisotropy is observed at the integral and Taylor scales in Rayleigh–Taylor turbulence, although the dynamics at the Kolmogorov microscale remain isotropic (Cabot & Zhou 2013). In these problems, the occurrence of anisotropy is attributable to both the presence of a large-scale density gradient across the mixing region and of an acceleration field. In particular, the relative alignment and magnitude of these vectors determines the stability of the Rayleigh–Taylor set-up and the amount of baroclinic vorticity generation. The acceleration field acts as a directional force term scaled by local density differences, and allows the flow to sustain anisotropy (Cook & Dimotakis 2001; Ristorcelli & Clark 2004; Livescu & Ristorcelli 2007). More specifically, in stably stratified turbulence, mixing due to the dispersion of light and heavy fluids by turbulence in the direction of gravity requires work to be done against buoyancy forces, which reduce the motions in this direction and thus lead to anisotropy (Turner 1968; Linden 1980). In Rayleigh–Taylor turbulence, an acceleration field and a density gradient are always both present; it is thus not possible to identify the individual contribution of each one to anisotropy. In cases when there is a gradient in composition as well, viscosities may be different in the two fluids, leading to a different turbulent kinetic energy dissipation rate. In addition, species diffusion in miscible fluids tends to locally smoothen the density gradient and consequently reduce the local rate of baroclinic vorticity production ($\sim \nabla \rho \times \nabla p$), compared with the immiscible counterpart. Thus, the dynamics in Rayleigh–Taylor turbulence are directly affected by the mixing process, by contrast to passive scalar (level 1) mixing. In addition, the kinematic viscosities in each fluid

may be different, such that the turbulence decays at different rates in each region, another source of anisotropy (Tordella & Iovieno 2011). Furthermore, non-Boussinesq effects become important at high Atwood numbers. Livescu & Ristorcelli (2007) studied turbulent mixing between two incompressible miscible fluids in an unstably stratified medium. The mean pressure evolves dynamically, as mixing occurs between the light and heavy fluids, leading to non-Boussinesq effects. In particular, Livescu & Ristorcelli (2008) and Livescu *et al.* (2010) state that the pure light fluid mixes faster than the pure heavy fluid, resulting in an asymmetric mixing process. These difficulties present challenges for investigating anisotropy in turbulent mixing through the Rayleigh–Taylor instability.

As our first step toward a better understanding of level 2 mixing in general and Rayleigh–Taylor turbulence in particular, we seek to isolate the effect of a density gradient from that of gravity on the turbulence. In contrast to past studies of Rayleigh–Taylor mixing, we start by neglecting gravity to consider passive scalar mixing, and subsequently superpose a density gradient on an initial isotropic field. Statistics of passive scalar mixing are known from numerical and experimental freely decaying (grid) turbulence studies (Warhaft 2000; Sawford 2001). In one such set of wind tunnel experiments, Jayesh, Tong & Warhaft (1994) and Tong & Warhaft (1994) used a conventional grid to generate an initial turbulent field with $30 \leqslant Re_\lambda \leqslant 130$, where Re_λ is the initial Taylor-scale Reynolds number, and imposed a linear mean cross-stream temperature gradient upstream of the grid. Due to the relatively low Mach number ($M \approx 0.017$) and negligible buoyancy effects over the time scales of interest, temperature can be assumed to behave as a passive scalar in those experiments in which the Schmidt number is 0.7. The scalar spectra in the inertial range approached the expected $-5/3$ slope sooner than those of velocity, and the dissipation of scalar variance was found to be 20 % larger in the direction of the temperature gradient. Mydlarski & Warhaft (1998) investigated higher Re_λ (up to 700) by employing an active grid technique to generate the initial turbulent field. Other passive scalar studies in grid turbulence focused on dispersion of a thermal wake behind a heated wire (Anand & Pope 1983; Warhaft 1984; Stapountzis *et al.* 1986), in which case the mean temperature profile was found to be Gaussian, while the variance was not. The mean thermal wake development was shown to consist of three stages: molecular diffusive ($h \sim t^{1/2}$), turbulent convective ($h \sim t$) and turbulent diffusive ($h \sim t^{1-n/2}$), where h is the mixing region width and n is the time exponent of the kinetic energy decay rate. However, the tunnel was not sufficiently long to reach the expected growth in the final stage. In the context of stably stratified turbulence, Huq & Britter (1995*a*) studied the role of Schmidt number on passive scalar mixing between two layers of different fluids due to grid-generated turbulence in water tunnel experiments. The scalar Taylor microscales were found to be dependent on the Schmidt number, whereas integral scales were not. Huq & Britter (1995*b*) also investigated the evolution of a mixing region starting from an initially sharp interface between two fluids of different densities. The mixing region grew initially due to turbulent diffusion, similar to the passive case, but at later times decreased because of buoyancy effects.

In the Richtmyer–Meshkov instability with reshock, a variable-density turbulent mixing region may develop (Hill, Pantano & Pullin 2006; Thornber *et al.* 2011; Tritschler *et al.* 2014). While the mixing region grows due to turbulence diffusion, the turbulence decays since no further energy feeds it (Drake 2006). In another related study, Lamriben, Cortet & Moisy (2011) investigated the role of background rotation on freely decaying turbulence in a water-filled rotating tank. By measuring

the anisotropic energy flux density and the energy distribution at different scales, Lamriben *et al.* (2011) observed in their experiments that anisotropy caused by rotation (i.e. Coriolis force) appears to result in small-scale anisotropy. This result lies in contrast with anisotropy observed in Rayleigh–Taylor turbulence, where the flow remains isotropic at small scales despite the large-scale anisotropy (Cabot & Zhou 2013).

Recent advances in numerical algorithms and supercomputers have allowed for the use of direct numerical simulation (DNS) to investigate turbulent mixing and compute flow statistics at relatively high Reynolds numbers. For instance, Livescu, Jaberi & Madnia (2000) performed DNS of the experiments of Warhaft (1984), with an emphasis on characterising the development of the scalar wake. Watanabe & Gotoh (2006, 2007) studied inertial-range intermittency under a mean scalar gradient in forced turbulence, focusing on scaling exponents of the structure functions of scalar increments. In freely decaying turbulence, anisotropy may be introduced by manipulating the initial distribution of kinetic energy even in the context of passive scalar mixing. For instance, Tordella & Iovieno (2006, 2011, 2012) used a problem set-up similar to that of the present work: two adjacent turbulent fields with the same or different integral scale and kinetic energy. When the energy dissipation rate was different in each field, departures from isotropy were found to be large, with higher intermittency in the direction of the kinetic energy gradient. At this time, no such studies of anisotropy caused by a density gradient alone have been reported.

In the present work, we seek to advance the fundamental understanding of level 2 turbulent mixing, by focusing on anisotropy caused by density and composition gradients alone in a freely decaying turbulent field with zero mean velocity. Our goal is to determine the extent to which the large-scale anisotropy in fluid density/composition modifies the phenomenology of the turbulence at different scales. We conduct DNS, in which all scales are resolved, using a novel set-up inspired by Tordella & Iovieno (2011): starting from passive scalar mixing in freely decaying turbulence with no external body force, we impose a density gradient by juxtaposing two fields of different densities. The key novelty lies in matching the kinematic viscosity and the initial turbulent kinetic energy per unit mass in the two fluids to ensure that the turbulence intensity starts at the same level and decays at the same rate in the two fluids, by contrast to Tordella & Iovieno (2011) who considered constant-density fields with different integral scales and kinetic energy. By doing so, we can isolate the effect of the density gradient alone. The rationale behind this strategy is that conventional turbulence scalings are based on kinetic energy per unit mass and kinematic viscosity, from which density and dynamic viscosity are absent. Thus, by matching the initial kinematics (root-mean-square velocity) and the corresponding dissipation (kinematic viscosity) in the two fluids, the turbulence decays at the same rate in the two fluids, even though there is an initial gradient in the kinetic energy (per unit volume). In our set-up, the density gradients are steep and initially localised. Sufficiently far away from the interface, the mean density is essentially uniform, such that the turbulence is expected to evolve isotropically. However, turbulence at the interface experiences an appreciable density gradient, such that within this region one expects the flow to behave anisotropically. The mechanisms responsible for anisotropy inside the mixing region are not immediately obvious; possibilities include the momentum of large-scale structures during entrainment and molecular diffusion at the small scales. The article is organised as follows. The problem description, including the governing equations, the numerical approach and the initial conditions are presented in §2. The large-scale dynamics are first investigated in §3, followed by a study of the small-scale dynamics in §4. The article concludes with a summary of the key points and an outlook for future work.

2. Problem description

2.1. *Physical model*

The three-dimensional compressible Navier–Stokes equations for a binary system of perfect gases describe the problem under consideration, which we solve numerically:

$$\frac{\partial \rho}{\partial t} + \frac{\partial}{\partial x_j}(\rho u_j) = 0, \tag{2.1}$$

$$\frac{\partial(\rho u_i)}{\partial t} + \frac{\partial}{\partial x_j}(\rho u_i u_j + p\delta_{ij}) = \frac{1}{Re}\frac{\partial \tau_{ij}}{\partial x_j}, \tag{2.2}$$

$$\frac{\partial E}{\partial t} + \frac{\partial}{\partial x_j}[u_j(E+p)] = \frac{1}{Re}\left[\frac{\partial}{\partial x_j}(u_i\tau_{ij}) + \frac{\partial}{\partial x_j}\left(k\frac{\partial T}{\partial x_j}\right) + \frac{1}{Sc}\frac{\partial}{\partial x_j}\left(\rho\frac{\partial Y_i}{\partial x_j}(h_1-h_2)\right)\right], \tag{2.3}$$

$$\frac{\partial(\rho Y_i)}{\partial t} + \frac{\partial(\rho u_j Y_i)}{\partial x_j} = \frac{1}{ReSc}\frac{\partial}{\partial x_j}\left(\rho\frac{\partial Y_i}{\partial x_j}\right), \tag{2.4}$$

where ρ is the density, p the pressure, u_i the velocity, $E = \rho(e + u_i u_i/2)$ the total energy per unit volume, $e = p/(\rho(\gamma - 1))$ the internal energy per unit mass, γ the specific heats ratio, T the temperature, Y_i the mass fraction of fluid i, k the thermal conductivity, $h = e + p/\rho$ the enthalpy, Re the scaled Reynolds number, Sc the Schmidt number and δ_{ij} the Kronecker delta. There are no body forces. The fluids are assumed Newtonian, with viscous stress tensor

$$\tau_{ij} = \mu\left[\left(\frac{\partial u_i}{\partial x_j} + \frac{\partial u_j}{\partial x_i}\right) - \frac{2}{3}\frac{\partial u_k}{\partial x_k}\delta_{ij}\right], \tag{2.5}$$

where μ is the viscosity. The viscosity and thermal conductivity of the mixture are determined from the Herning and Zipper (Reid, Prausnitz & Poling 1987) approximation for a binary mixture:

$$\mu = \frac{\mu_1 Y_1 M_1^{-1/2} + \mu_2 Y_2 M_2^{-1/2}}{Y_1 M_1^{-1/2} + Y_2 M_2^{-1/2}}, \tag{2.6}$$

where M is the molecular weight. The ideal gas equation for a binary mixture reads

$$\frac{p}{\rho} = RT, \quad \text{with} \quad \frac{1}{M} = \frac{Y_1}{M_1} + \frac{Y_2}{M_2}, \tag{2.7}$$

where $R = \bar{R}/M$ is the gas constant and $\bar{R}$ the universal gas constant. In general, the two fluids may take on different densities, pressures, temperatures, molecular weights, viscosities and thermal conductivities.

In our problem, the specific heats ratio γ is set to 1.4 in both fluids. The light-fluid density ρ_1, the length $l = L/(2\pi)$ where L is the computational domain width, the velocity $u_{ref} = 1$, the pressure $p_{ref} = \rho_1 u_{ref}^2$ and the light-fluid gas constant $R_{ref} = R_1$ are used for non-dimensionalisation. The Schmidt and Prandtl numbers are related to the scaled variables by

$$Sc = \frac{\mu_1}{\rho_1 D}, \quad Pr = \frac{c_p \mu}{k}, \tag{2.8a,b}$$

where D is the mass diffusivity, and c_p is the specific heat at constant pressure, which can be written in terms of R and γ as

$$c_p = \frac{\gamma}{\gamma - 1}R. \tag{2.9}$$

For simplicity, we set $\mu_1 = 1$ and define the scaled Reynolds number, *Re*, later in (2.14) based on the Taylor-scale Reynolds number.

2.2. *Numerical method*

We use explicit finite differences in space to numerically solve the equations of motion listed in the previous section. A sixth-order central scheme in the split form approximates the convective fluxes. No artificial dissipation is necessary since the mesh resolutions are sufficiently high to resolve the steep (but not discontinuous) density and mass fraction gradients, as described in § 2.4. As shown in Movahed & Johnsen (2013*a*), the advection terms of (2.1) are expanded based on the form of Blaisdell, Spyropoulos & Qin (1996):

$$\frac{\partial}{\partial x_j}(\rho u_j \phi) = \frac{1}{2}\frac{\partial}{\partial x_j}(\rho u_j \phi) + \frac{1}{2}u_j\frac{\partial}{\partial x_j}(\rho \phi) + \frac{1}{2}\rho\phi\frac{\partial u_j}{\partial x_j}, \tag{2.10}$$

where $\phi = (1, u_i, (E + p)/\rho, Y_i)$. The flux of Ducros *et al.* (2000) is implemented in the split form, which satisfies summation by parts in periodic domains and is discretely conservative. This approach minimises unphysical pile-up of energy at high wavenumbers due to potential aliasing errors. Diffusive terms are discretised in non-conservative form as

$$\frac{\partial}{\partial x}\left(\mu\frac{\partial u}{\partial x}\right) = \mu\frac{\partial^2 u}{\partial x^2} + \frac{\partial \mu}{\partial x}\frac{\partial u}{\partial x}, \tag{2.11}$$

resulting in better accuracy, robustness, spectral representation of diffusive effects at high wavenumbers and preventing odd–even decoupling (Pirozzoli 2011). A third-order accurate explicit strong stability preserving (SSP) Runge–Kutta scheme is used for time marching (Gottlieb & Shu 1998). This approach has been used to investigate late-time mixing in the Richtmyer–Meshkov instability (Movahed & Johnsen 2011, 2013*a*).

2.3. *Single-fluid freely decaying isotropic turbulence*

We first consider decaying isotropic turbulence in a single fluid, which constitutes the basis for the initialisation of our multifluid problem. The initial conditions consist of a random solenoidal velocity field inside a triple periodic box of size $2\pi \times 2\pi \times 2\pi$ that satisfies a Batchelor spectrum $E(k) \sim k^4 \exp(-2k^2/k_0^2)$, where k_0 is the most energetic wavenumber and $\lambda_0 = 2/k_0$ is the initial Taylor microscale (Batchelor & Proudman 1956; Lee, Lele & Moin 1991; Johnsen *et al.* 2010; Movahed & Johnsen 2013*b*). The density and pressure fields are initially uniform. The turbulent Mach number and Taylor-scale Reynolds number are defined as

$$M_t = \frac{\sqrt{\langle u_i u_i \rangle_{vol}}}{\langle c \rangle_{vol}}, \quad Re_\lambda = \frac{\langle \rho \rangle_{vol} u_{rms} \lambda}{\langle \mu \rangle_{vol}}, \tag{2.12a,b}$$

where

$$u_{rms} = \sqrt{\frac{\langle u_i u_i \rangle_{vol}}{3}}, \quad \lambda^2 = \frac{\langle u_i^2 \rangle_{vol}}{\left\langle \left(\frac{\partial u_i}{\partial x_i}\right)^2 \right\rangle_{vol}}. \tag{2.13a,b}$$

Here, c is the sound speed, λ is the time-varying Taylor microscale, and $\langle \cdot \rangle_{vol}$ denotes spatial averages over the whole domain. An important time scale of the problem is the eddy turnover time defined based on the initial properties, $\tau = \lambda_0/u_{rms,0}$. We relate the initial Taylor-scale Reynolds number, $Re_{\lambda,o}$, and the scaled Reynolds number, Re, as

$$Re_{\lambda,o} = Re \left[\frac{\rho_0 u_{rms,0} \lambda_0}{\mu} \right]. \tag{2.14}$$

The same approach as that discussed in detail in Johnsen *et al.* (2010) is used to generate the initial random field on the finest grid. For a given k_0, the velocity field is generated on the finest mesh ($N^3 = 512^3$) and spectrally filtered to coarser grids. We show sample results for simulations with $k_0 = 4$, $Re_{\lambda,o} = 60$–200, and $M_t = 0.1$ in figure 1. During an initial transition period (up to 2–3τ), the energy is redistributed across scales by nonlinear energy transfer mechanisms, resulting in a state of turbulence. Since the initial conditions are not in acoustic equilibrium, pressure fluctuations develop from the initial field as the pressure becomes consistent with the velocity (Ristorcelli & Blaisdell 1997). The enstrophy increases as the fluctuations representing the different turbulent modes (acoustic, vorticity and entropy) reach this equilibrium state (Monin & Yaglom 1975). The skewness of velocity derivatives, defined as

$$S = \frac{\left\langle \frac{1}{3} \left(\frac{\partial u_i}{\partial x_i} \right)^3 \right\rangle_{vol}}{\left\langle \frac{1}{3} \left(\frac{\partial u_i}{\partial x_i} \right)^2 \right\rangle_{vol}^{1.5}}, \tag{2.15}$$

is a measure of the nonlinear equilibrium of turbulence; in our simulations, it ranges between -0.6 and -0.4 at $Re_{\lambda,o} = 60$–200, in agreement with previously reported values for physically realistic turbulence (Sreenivasan & Antonia 1997). Since there is no external forcing providing energy to the turbulence, the total kinetic energy decays due to viscous diffusion, as exemplified by the decrease in turbulent Mach number. As is the case in many past numerical studies of this problem (Lee *et al.* 1991; Larsson & Lele 2009; Johnsen *et al.* 2010; Bhagatwala & Lele 2011, 2012), the Reynolds numbers do not remain over 100 for an extensive time in our simulations, such that the turbulence is not fully developed based on the definition of Dimotakis (2000). In this sense, we do not expect our results to be Reynolds-number independent. Although shocklets may form at sufficiently high M_t and thus require shock capturing, the present focus is on $M_t < 0.4$ (Samtaney, Pullin & Kosovic 2001); for the present turbulent Mach numbers, central differences can be used in a stable fashion everywhere for all time. Turbulent kinetic energy spectra for $Re_{\lambda,o} = 100$, $M_t = 0.1$ and $t = 4\tau$ are shown in figure 2 for different grid resolutions. These results confirm that the dynamics of all turbulent scales are accurately represented on a grid of $N^3 = 256^3$, which is used for most of the present simulations.

2.4. *Initial set-up for the multifluid simulations*

2.4.1. *Domain and initial mass fraction field*

The computational domain consists of a rectangular parallelepiped of size $L \times L \times 10L$, with $L = 2\pi$ and N points per L on a uniform Cartesian grid (figure 3). The velocity field described in § 2.3 is used to initialise the problem. Taking advantage
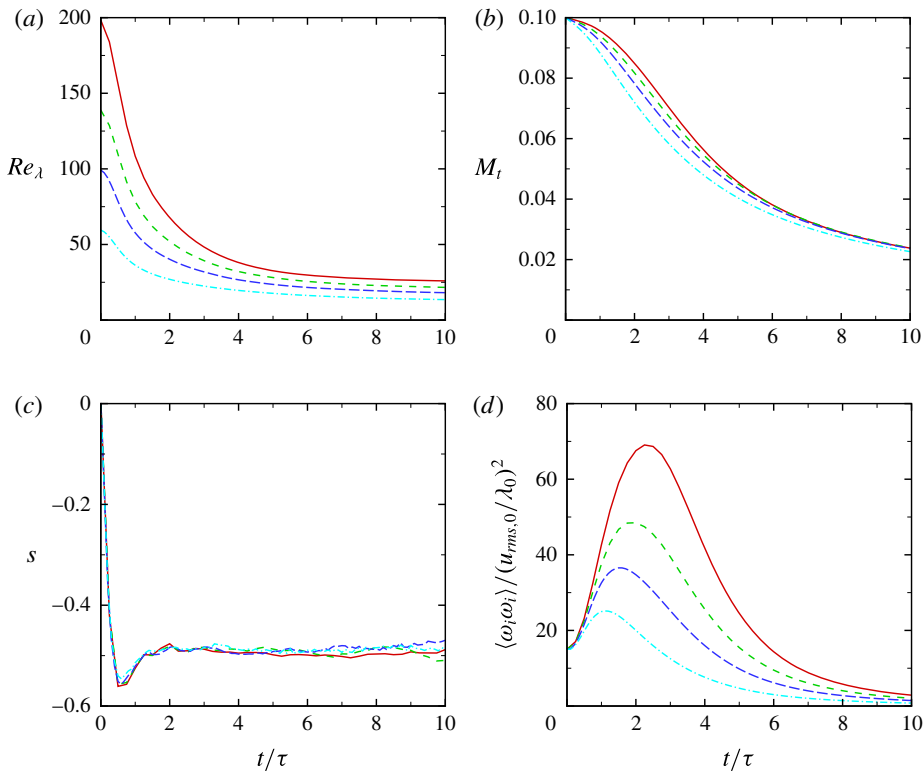
FIGURE 1. (Colour online) Temporal evolution of Re_λ (*a*), M_t (*b*), skewness (*c*) and enstrophy (*d*) for single-fluid decaying isotropic turbulence at $Re_{\lambda,o} = 60$ (dot-dashed, cyan), 100 (long dashed, blue), 140 (short dashed, green) and 200 (solid, red).
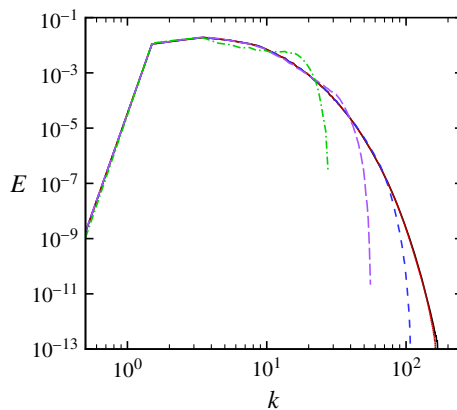

FIGURE 2. (Colour online) Kinetic energy spectra for single-fluid decaying isotropic turbulence at $t = 4\tau$, with $Re_{\lambda,o} = 100$, $M_t = 0.1$, and $N^3 = 32^3$ (dot-dashed, green), 64^3 (long dashed, purple), 128^3 (short dashed, blue), 256^3 (dotted, red), 512^3 (solid, black), where N is the number of grid points per domain width. Note that the red and black curves lie on top of each other.
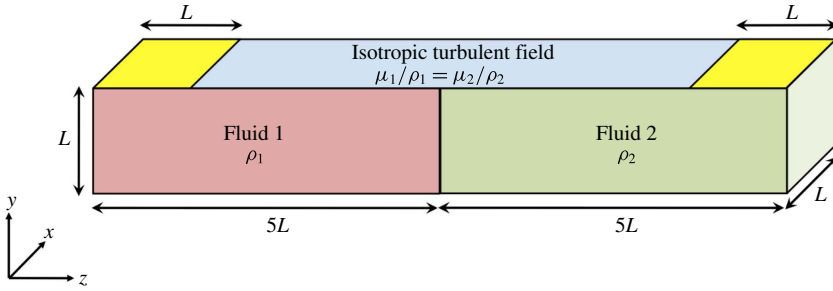
FIGURE 3. (Colour online) Schematic of the initial computational set-up (not to scale). Two fluids of different densities are initially separated by a diffuse unperturbed material interface in the presence of a random initial velocity field that evolves to turbulence. The turbulence is damped in the yellow region to avoid numerical errors at the non-reflecting boundaries.

of periodicity, 10 such isotropic boxes are juxtaposed in the z direction to make up the full domain. Boundary conditions are periodic in the x and y directions, and non-reflecting with one-sided differences in the z direction. Although the approach of Thompson (1987) is followed for non-reflecting conditions, numerical errors may be generated as turbulence reaches the boundaries. To avoid such difficulties, an error function is used to damp the turbulent fluctuations near the boundaries. The length of the domain ($10L$) in the z direction is selected to ensure that boundaries have a negligible effect on the evolution of the mixing region near $z = 0$.

To prevent generation of unphysical waves at the interface in the presence of finite physical mass diffusion, the following mean velocity is prescribed at the interface (Joseph 1990; Cook & Dimotakis 2001; Movahed 2014),

$$u_i = -\frac{1}{Re\,Sc} \frac{1}{\rho} \frac{\partial \rho}{\partial x_i}. \tag{2.16}$$

While the initial volume-averaged velocity is homogeneous and isotropic, inhomogeneity is introduced in the form of composition and density gradients in the z direction. The initial mass fraction field is generated without any perturbations in the x–y plane:

$$Y_1(z) = \frac{1}{2}\left[1 - \mathrm{erf}\left(\frac{z - z_0}{H}\right)\right], \tag{2.17}$$

where $z_0 = 0$ is the mid-plane location separating the two fluids corresponding to $Y_1 = 0.5$. The value $H = 8/128L$ corresponds to the steepest interface profile that central differences are capable of resolving in a satisfactory fashion on a $N = 128$ points per L grid, thus avoiding the use of shock capturing and minimising numerical dissipation that would otherwise overwhelm the small turbulent scales (Johnsen *et al.* 2010). Because of this, the mixing region has a finite initial size. For simplicity, we keep the ratio of the initial thickness of the mixing region to the initial Taylor microscale constant for all simulations. In the current set-up, pressure is uniform initially. To achieve an isothermal field and minimise compressibility effects, the properties of the heavy and light fluids are related as follows (Dimonte *et al.* 2004):

$$\frac{R_2}{R_1} = \frac{M_1}{M_2} = \frac{\rho_1}{\rho_2}, \quad p_{initial} = T_{initial} = 2\pi L(\rho_1 + \rho_2). \tag{2.18a,b}$$
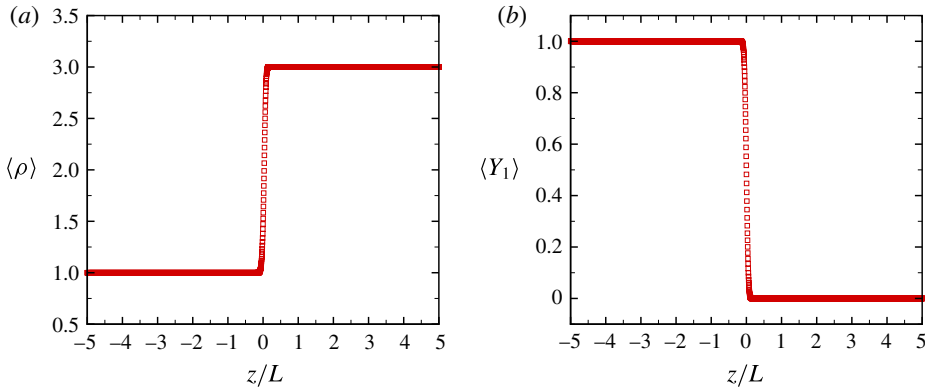
FIGURE 4. (Colour online) Initial mass fraction (*a*) and density (*b*) fields for $N = 256$ per L and $\rho_2/\rho_1 = 3$.

In the mixing region, the initial density profile is obtained from the mass fraction field (Cook & Dimotakis 2001):

$$\frac{1}{\rho} = \frac{Y_1}{\rho_1} + \frac{Y_2}{\rho_2}. \tag{2.19}$$

Figure 4 shows the initial mass fraction and density fields for $\rho_2/\rho_1 = 3$.

2.4.2. *Matched dissipation rate and key dimensionless parameters*

The important parameters in the heavy and light fluids are related as follows:

$$\frac{Re_{\lambda 2}}{Re_{\lambda 1}} = \frac{\rho_2 \mu_1}{\rho_1 \mu_2}, \quad M_{t2} = M_{t1} \sqrt{\frac{\rho_2}{\rho_1}}, \tag{2.20a,b}$$

with $M_{t1} = 0.1$. Due to the non-dimensionalisation, the turbulent Mach number is slightly different in each fluid, but since dilatational dissipation is negligible this discrepancy is not expected to affect the dynamics. Simulations are performed at a Prandtl number of 0.7 and Schmidt number 1.0.

The fluids have different densities and dynamic viscosities such that the kinematic viscosities are the same in both fluids, i.e. $\mu_1/\rho_1 = \mu_2/\rho_2$. Since the velocity is initialised with the same random field in each fluid, the initial Taylor-scale Reynolds numbers are the same in both fluids. Furthermore, we expect the integral quantities representative of the turbulence dynamics, e.g. dissipation rate, enstrophy and turbulent kinetic energy per unit mass, and relevant length scales (Taylor and Kolmogorov microscales) to evolve in the same fashion in each fluid, except perhaps in the mixing region (Samtaney *et al.* 2001; Movahed & Johnsen 2013*b*). Therefore, the initial conditions exhibit anisotropy solely in the composition and density gradients. Figure 5 confirms that the kinetic energy per unit mass $\langle u_i u_i \rangle$ and enstrophy remain nearly uniform in the entire domain apart from slight changes in the mixing region for a density ratio of 3:1. Since it is not possible to simultaneously match the kinetic energy per unit mass and the kinetic energy per unit volume $\langle \rho u_i u_i \rangle$ when considering fluids of different densities, we choose to match the kinetic energy per unit mass in this study. The rationale behind this strategy is that conventional turbulence scalings are based on kinetic energy per unit mass and kinematic viscosity, such that density and dynamic viscosity do not appear. Thus, by matching the initial kinematics (kinetic
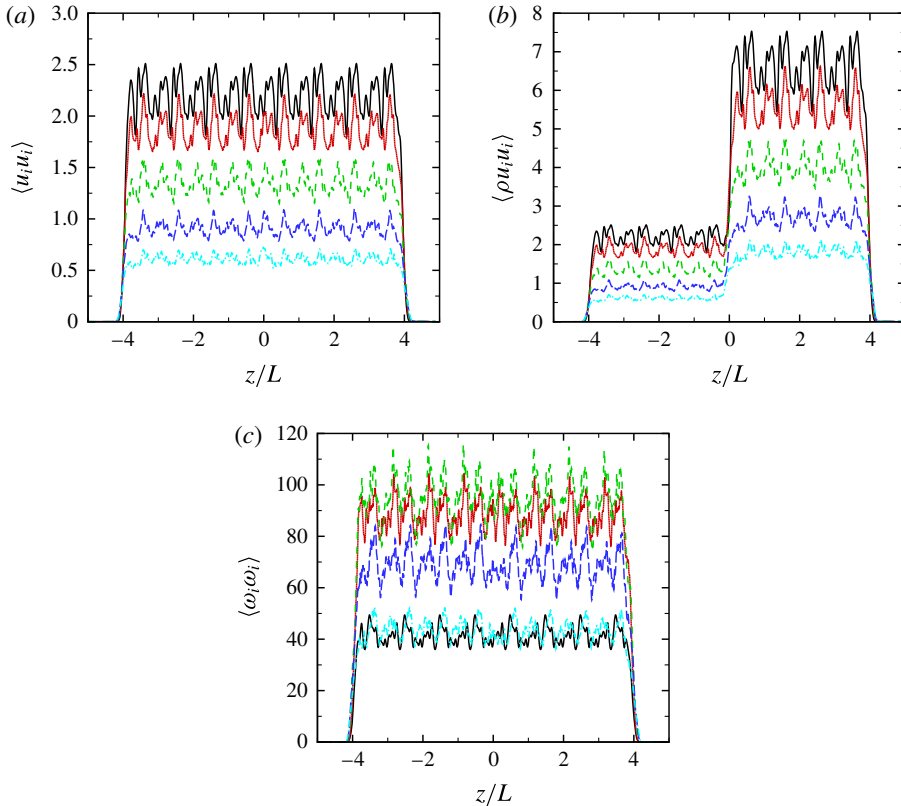
FIGURE 5. (Colour online) Spatial distribution of the kinetic energy per unit mass and per unit volume and enstrophy in the x–y plane during the first four eddy turnover times for $Re_{\lambda,o} = 100$, $\rho_2/\rho_1 = 3$, and $t/\tau = 0$ (solid, black), 1 (dotted, red), 2 (short dashed, green), 3 (long dashed, blue) and 4 (dot-dashed, cyan).

energy per unit mass) and the corresponding dissipation (kinematic viscosity) in the two fluids, the turbulence decays at the same rate in the two fluids, even though there is an initial gradient in the kinetic energy (per unit volume). The present problem set-up to investigate the role of density gradient alone is justified by the nearly homogeneous kinetic energy per unit mass and enstrophy in figure 5, even across the mixing region. The density difference across the interface manifests itself as a gradient in the turbulent kinetic energy per unit volume across the mixing region, as shown in figure 5. This gradient in the mass-averaged kinetic energy across the mixing region decreases as turbulence decays.

To show that the turbulence dynamics are similar at different densities, we conduct two simulations of single-fluid decaying isotropic turbulence, one with an initial uniform density of one and another with an initial uniform density of three. The respective viscosities are chosen such that $Re_{\lambda,o} = 100$ in both simulations. These two simulations correspond to freely decaying turbulence in the multifluid set-up with a density ratio of three away from the interface in the light and heavy fluids. Figure 6 shows the temporal evolution of volume-averaged kinetic energy per unit mass, enstrophy, Taylor microscale, and velocity spectra at $t/\tau = 10$. These results confirm that by matching the kinematic viscosity the turbulence, created by the initial
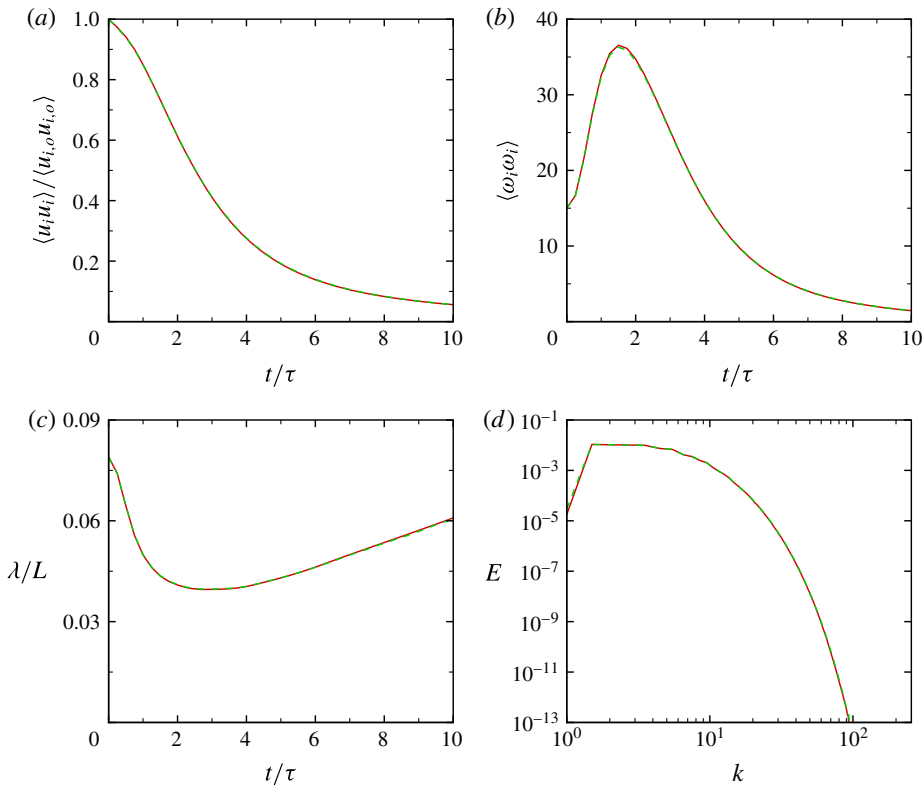
FIGURE 6. (Colour online) Temporal evolution of normalised kinetic energy per unit mass, enstrophy and Taylor microscale, and kinetic energy spectra at $t/\tau = 10$ for $Re_{\lambda,o} = 100$, and initial densities of 1 (solid, red) and 3 (dashed, green) with the same kinematic viscosity.

field behaves in the same fashion in a light and in a heavy fluid. The slight difference between the two results is due to the different initial turbulent Mach numbers (2.20).

In our simulations, the quantities that we vary are the density ratio, $\rho_2/\rho_1 = 1$, 3, 5, 8 and 12, and the initial Reynolds numbers, $Re_{\lambda,o} = 60$, 100, 120, 140 and 200. A density ratio of $\rho_2/\rho_1 = 1$ corresponds to passive scalar mixing, since the other relevant fluid properties are identical. Table 1 summarises the simulations runs, along with the relevant flow parameters.

3. Results: dynamics of the large scales in the mixing region

The focus of this section lies in the large-scale dynamics of the mixing region. First, the qualitative behaviour is presented (§ 3.1). For different density ratios, we consider the evolution of the mixing region width in § 3.2, followed by analysis based on the observation that the growth is self-similar (§ 3.3). We finally assess how well mixed the fluids are in § 3.4.

3.1. *Qualitative behaviour of the large scales*

We begin by considering the qualitative behaviour of the velocity and mass fraction fields. Figure 7 shows instantaneous three-dimensional visualisations of the evolution
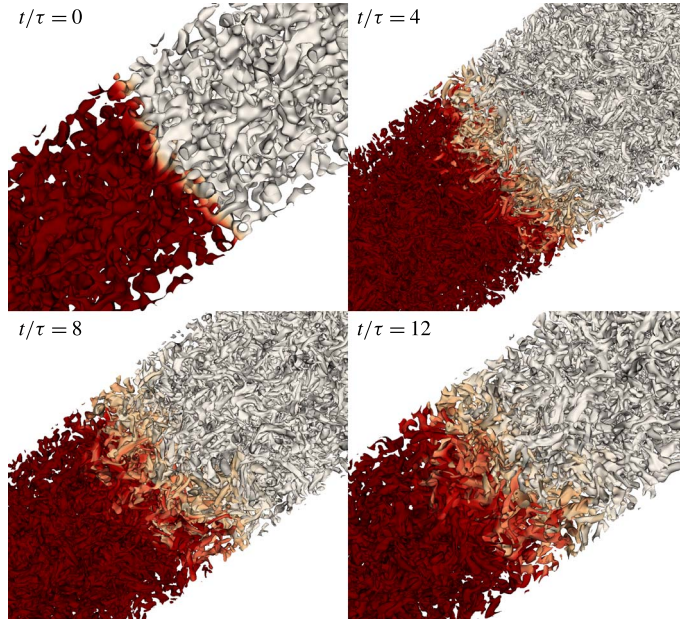
FIGURE 7. (Colour online) Snapshots of turbulent eddies extracted by the normalised Q-criterion coloured by mass fraction for $Re_{\lambda,o} = 100$ and $\rho_2/\rho_1 = 3$. Dark red, light fluid (bottom left); white, heavy fluid (top right).

Mixing classification	ρ_2/ρ_1	μ_2/μ_1	k_o	$Re_{\lambda,i}$	N
Level 1	1	1	4	60, 100, 120, 140	256
Level 1	1	1	4	200	512
Level 1	1	1	8	60, 100, 140	512
Level 2	3	3	4	60, 100, 120, 140, 200	256
Level 2	5	5	4	60, 100	256
Level 2	8	8	4	60, 100	256
Level 2	12	12	4	60	256
Level 2	12	12	4	100	512

TABLE 1. Summary of the DNS runs with the relevant flow parameters.

of the turbulent field and mixing region for $\rho_2/\rho_1 = 3$ and $Re_{\lambda,o} = 100$, where Re_λ is the initial Taylor-scale Reynolds number. The normalised Q-criterion is defined as

$$\Lambda = \frac{S_{ij}^* S_{ij}^* - \frac{1}{2}\omega_k\omega_k}{S_{ij}^* S_{ij}^* + \frac{1}{2}\omega_k\omega_k}, \tag{3.1}$$

where $\boldsymbol{\omega} = \nabla \times \boldsymbol{u}$ is the vorticity and

$$S_{ij}^* = S_{ij} - \frac{\delta_{ij}}{3} S_{kk}, \quad S_{ij} = \frac{1}{2}\left(\frac{\partial u_i}{\partial x_j} + \frac{\partial u_j}{\partial x_i}\right), \tag{3.2}$$

where S_{ij} is the strain-rate tensor. The Q-criterion is used to extract approximate outlines of the turbulent eddies and visualise changes in their morphology. In addition,

the eddies are coloured by mass fraction to highlight the dynamics and growth of the mixing region. Over the first few eddy turnover times, ever smaller scales are produced as the energy is redistributed across wavenumbers and the initial random field evolves to turbulence. At late times, the smaller eddies have dissipated, leaving the largest ones behind (Pope 2000). The mixing region grows with time through a turbulent diffusion process, in which heavy eddies near the interface are entrained and dispersed into the light fluid, and vice versa. There is no clear qualitative difference between the size and dynamics of eddies at any fixed time in the flow. Similar observations can be made by considering instantaneous two-dimensional slices of mass fraction in figures 8 and 9. As the Reynolds number is increased, smaller-scale features are discernible at a given time; however, it is not immediately clear how the Reynolds number affects the mixing region growth rate. A larger density ratio does not appear to significantly affect the size distribution of the turbulent length scales qualitatively. However, the mean location of the mixing region changes in the plots for different density ratios; the heavier fluid displaces the lighter. In addition, this process appears to produce a wider mixing region. Although such qualitative results provide useful information, more quantitative measures are necessary, which are investigated in greater detail in the following sections.

3.2. *Evolution of the mixing region width*

The dynamics in the mixing region are of particular interest, so instantaneous mean profiles of mass fraction are first examined. As the fluids mix, the width of the mixing region grows with time. The temporal evolution of the mass fraction varies with density ratio, as shown in figure 10. More importantly, the mid-plane corresponding to $\langle Y \rangle = 0.5$, where $\langle \cdot \rangle$ denotes spatial averages in x–y, shifts toward the lighter fluid as the density ratio is increased; we discuss this phenomenon in more detail at the end of this section. This result is important in the context of the Rayleigh–Taylor instability, as the temporal evolution of turbulence statistics is often reported at a fixed location relative to the grid, namely the $z = 0$ plane (Cook & Dimotakis 2001). The mass fraction is essentially antisymmetric about $\langle Y \rangle = 0.5$ at low-density ratios, but loses this property as the density ratio increases.

We measure the mixing region growth using two approaches. The first, borrowed from Rayleigh–Taylor instability analysis, is based on the notion of spikes/bubbles (masses of heavy/light fluids penetrating the light/heavy fluids). The spike (bubble) amplitude h_s (h_b) is defined as the distance between $\langle Y_1 \rangle \leqslant 0.99$ ($\langle Y_1 \rangle \geqslant 0.01$) and the initial mid-plane ($z = 0$). The spikes (bubbles) amplitude growth is due to the penetration of the heavy (light) fluid into the light (heavy) fluid. The amplitude of the mixing region, h_{amp} is defined as the average of h_b and h_s:

$$h_{amp} = \frac{h_s + h_b}{2}. \tag{3.3}$$

Figure 11 shows that over the first two to three eddy turnover times different density ratios do not produce very different h_s or h_b; this observation can be related to the initial thickness of the unperturbed interface at $t = 0$. Since the initial Taylor microscale is on the order of the initial interface thickness, it takes finite time for the eddies in the pure heavy fluid to penetrate the pure light fluid and contribute to spike growth. This behaviour occurs sooner for simulations with an initially thinner interface (figure 12), in which case the role of the density gradient on the bubble and spike growth becomes evident from earlier times. After the first two to
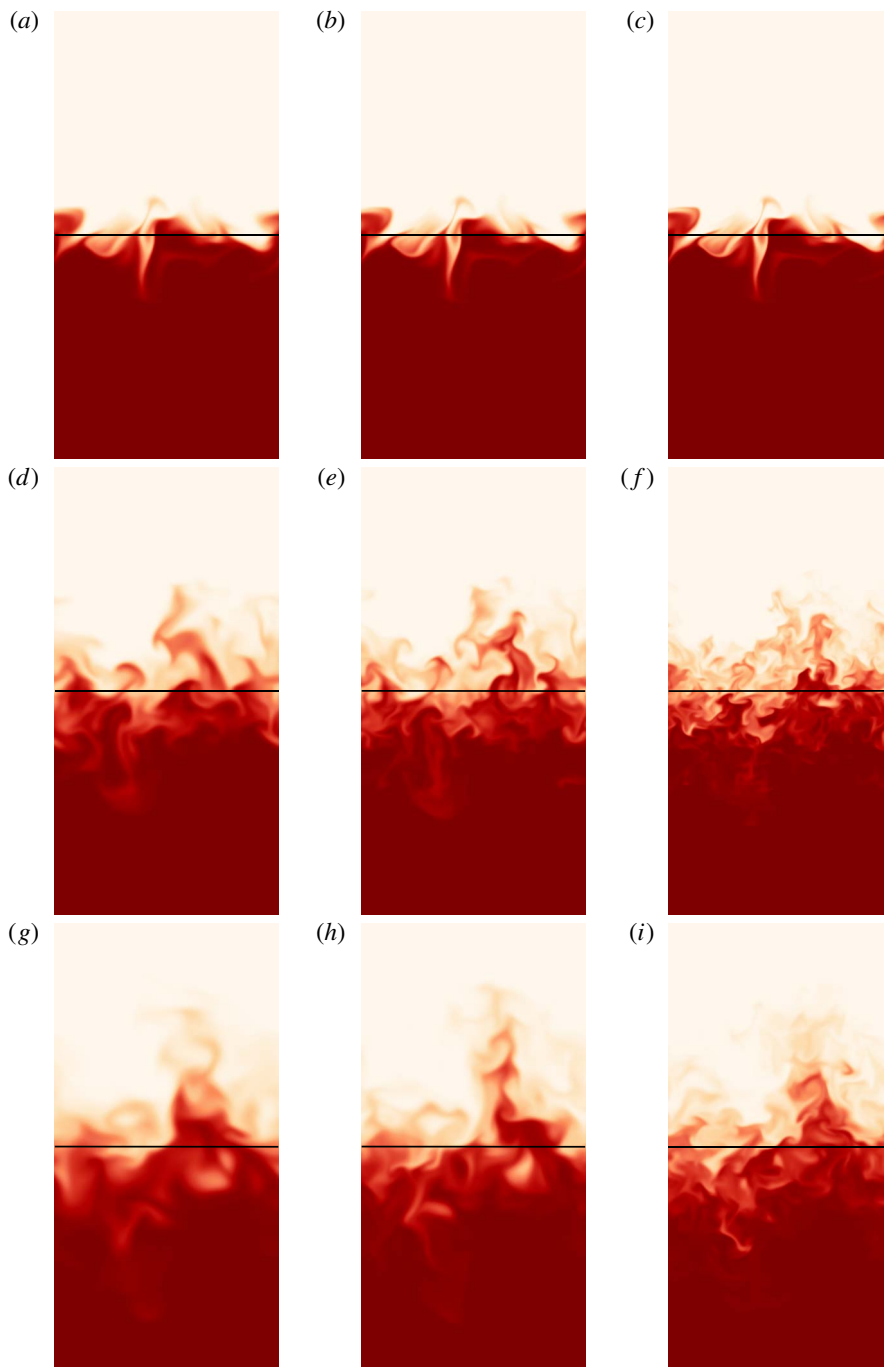
FIGURE 8. (Colour online) Two-dimensional contours of mass fraction in the x–z plane at $t = 1\tau$ (a,b,c), $t = 5\tau$ (d,e,f) and $t = 10\tau$ (g,h,i) for $\rho_2/\rho_1 = 1$ and $Re_{\lambda,o} = 60$ (a,d,g), 100 (b,e,h) and 200 (c,f,i). The vertical direction corresponds to the direction of anisotropy in the composition (z direction). Each plot covers an area of $L \times 2L$ and the initial mid-plane ($z = 0$) is located in the middle of the vertical direction. Dark red, light fluid (bottom); white, heavy fluid (top); black line, initial $z = 0$ plane.
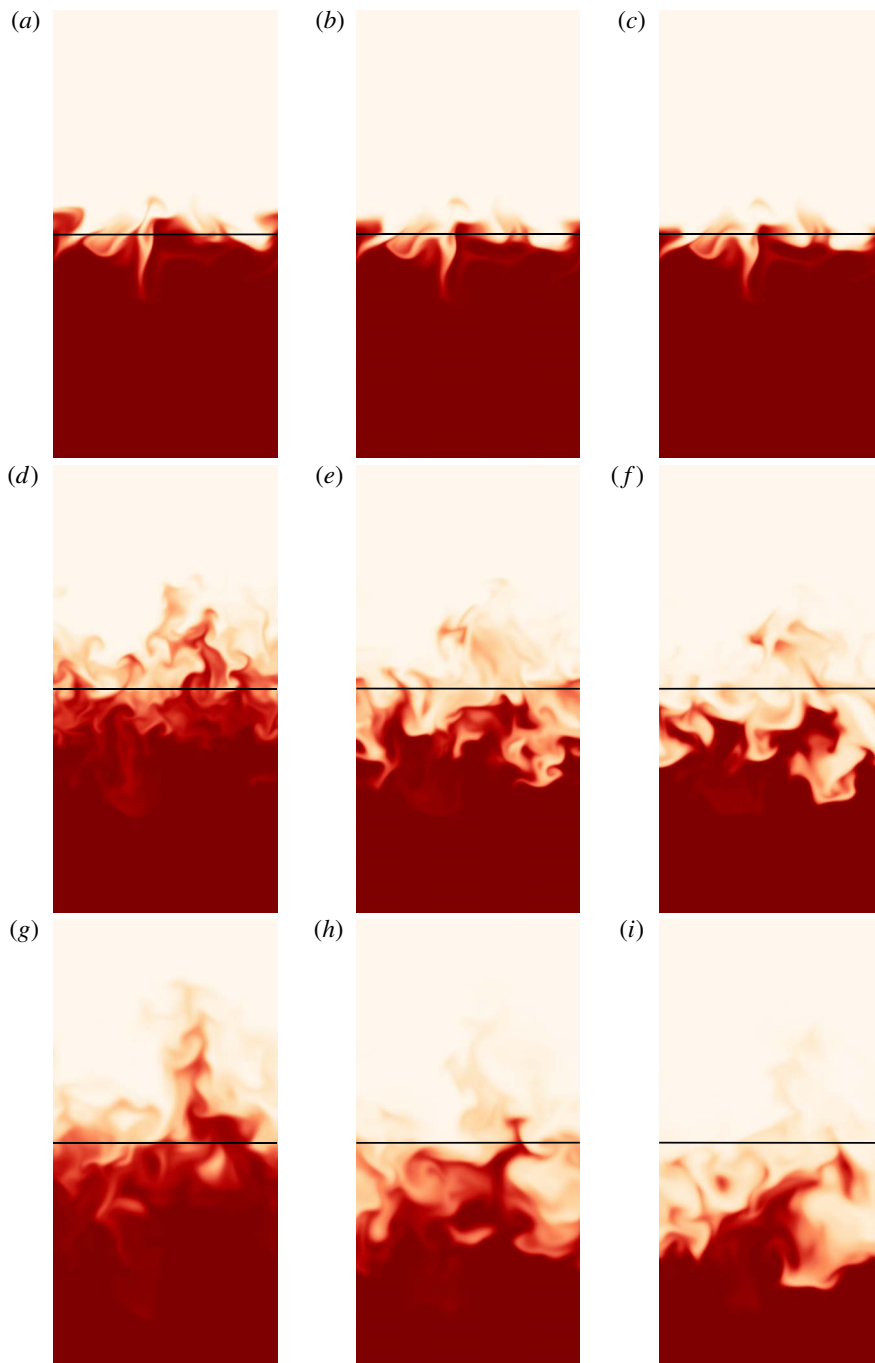
FIGURE 9. (Colour online) Two-dimensional contours of mass fraction in the x–z plane at $t = 1\tau$ (a–c), $t = 5\tau$ (d–f) and $t = 10\tau$ (g-i) for $Re_{\lambda,o} = 100$ and $\rho_2/\rho_1 = 1$ (a,d,g), 5 (b,e,h) and 12 (c,f,i). The vertical direction corresponds to the direction of anisotropy in the composition (z direction). Each plot covers an area of $L \times 2L$ and the initial mid-plane ($z = 0$) is located in the middle of the vertical direction. Dark red, light fluid (bottom); white, heavy fluid (top); black line, initial $z = 0$ plane.
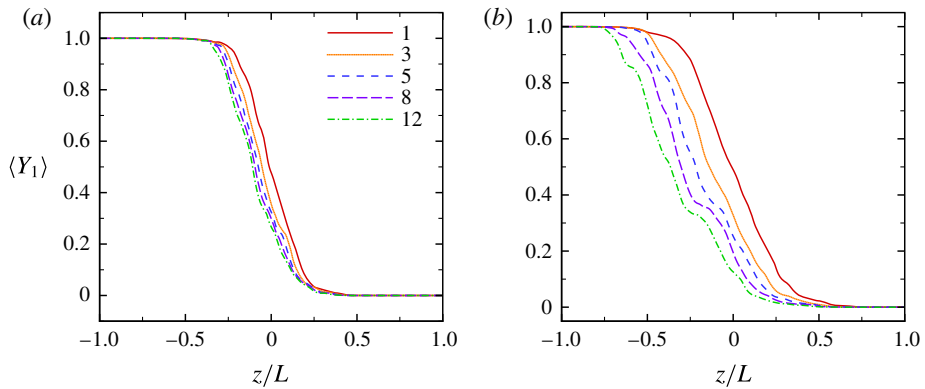
FIGURE 10. (Colour online) Mass fraction profiles at $t = 3\tau$ (*a*) and $t = 10\tau$ (*b*) for $Re_{\lambda,o} = 100$, and $\rho_2/\rho_1 = 1$ (solid, red), 3 (dotted, orange), 5 (short dashed, blue), 8 (long dashed, purple) and 12 (dot-dashed, green).
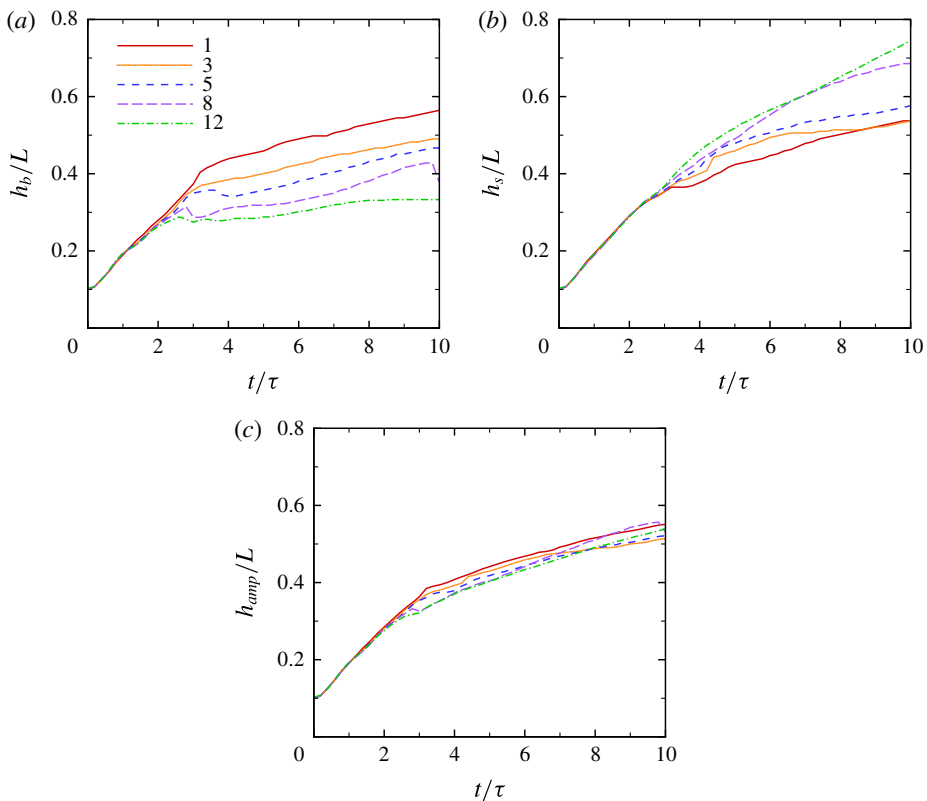

FIGURE 11. (Colour online) Temporal evolution of (*a*) h_b, (*b*) h_s and (*c*) h_{amp} for $Re_{\lambda,o} = 100$, and $\rho_2/\rho_1 = 1$ (solid, red), 3 (dotted, orange), 5 (short dashed, blue), 8 (long dashed, purple) and 12 (dot-dashed, green).
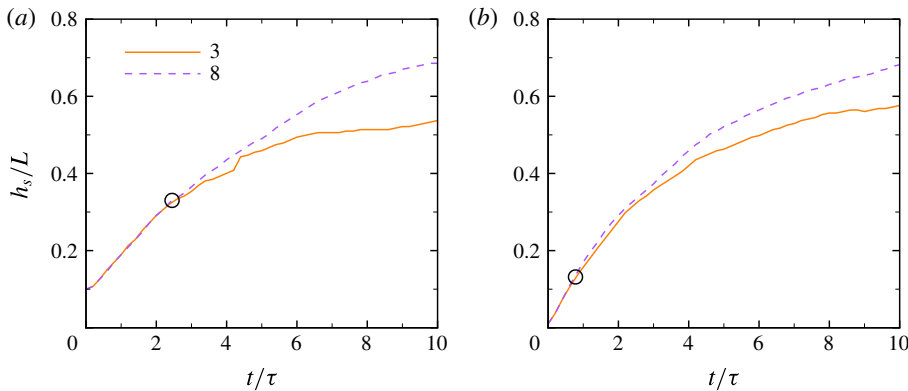
FIGURE 12. (Colour online) Temporal evolution of spike amplitude for $Re_{\lambda,o} = 100$, $\rho_2/\rho_1 = 3$ (solid, orange) and 8 (dashed curve, purple) for different initial thicknesses H as defined in (2.17): (a) $H = 8/128L$, used in the rest of the article; (b) $H = 1/128L$.

three eddy turnover times, the growth of the bubbles and spikes strongly depend on the density ratio (figure 11). The increase in spike amplitude can be explained via momentum considerations. In the absence of gravity and with increasing ρ_2/ρ_1, an eddy in the heavy fluid has higher momentum than the corresponding volume of light fluid, such that it is easier for the heavy fluid to displace the light fluid and penetrate it. The same dependence on the density ratio (through the Atwood number) has been observed in Rayleigh–Taylor instability (Cook & Dimotakis 2001). The asymmetry in bubble/spike growth in the absence of gravity suggests that such momentum considerations are important factors in the asymmetric growth observed in Rayleigh–Taylor instability as ρ_2/ρ_1 is increased, rather than gravity effects alone. As a result, the mean position of the interface moves toward the light fluid. This motion is greater for higher density ratio, an observation confirmed by monitoring the location in z of the $\langle Y \rangle = 0.5$ plane (figure 13). To illustrate this point, we extend the analysis of Tordella, Iovieno & Bailey (2008) to variable-density flows. Assuming that the dilatation is small in our problem, the averaged momentum equations can be written

$$\frac{\partial \overline{\rho u_i}}{\partial t} + \frac{\partial}{\partial x_j} \overline{\rho u_i u_j} = -\frac{\partial \bar{p}}{\partial x_j} + \frac{\partial}{\partial x_j} \overline{\left(\mu \frac{\partial u_i}{\partial x_j} \right)}, \tag{3.4}$$

where the bars denote the mean. Since there is no mean pressure gradient, the z-momentum equation for the mean reduces to

$$\frac{\partial}{\partial t} \overline{\rho w} = -\frac{\partial}{\partial z} \overline{\rho w^2} + \frac{\partial}{\partial z} \overline{\mu \frac{\partial w}{\partial z}}. \tag{3.5}$$

Initially, the mean momentum is zero. Since the last term is diffusive, the mean momentum in the z direction becomes negative for a positive density gradient, such that the mean interface location moves in the negative z direction, thus confirming the simulations results. Over the range $1 \lesssim t/\tau \lesssim 4$, the mean interface location appears to move at an approximately constant velocity proportional to the Atwood number, although the explicit dependence is not straightforward. While this motion results in a greater asymmetry in bubble and spike as the density ratio increases, it does not have a clear effect on the total mixing width ($2h_{amp}$) as the asymmetry is de-emphasised
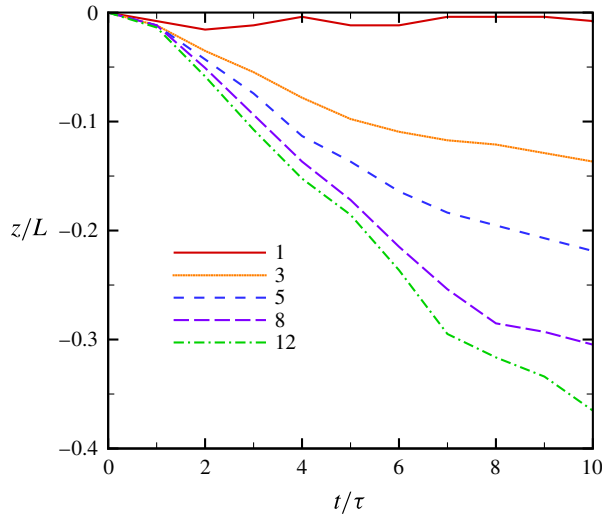
FIGURE 13. (Colour online) Temporal evolution of the $\langle Y \rangle = 0.5$ plane in z for $Re_{\lambda,o} = 100$, and $\rho_2/\rho_1 = 1$ (solid, red), 3 (dotted, orange), 5 (short dashed, blue), 8 (long dashed, purple) and 12 (dot-dashed, green).

when averaging the bubble and spike growth in (3.3). For $4 \lesssim t/\tau \lesssim 6$, the higher density ratios lead to a smaller h_{amp}; no clear pattern emerges thereafter.

The second measure of mixing region width is defined as

$$h = 2 \int_{-\infty}^{\infty} \min(\langle Y_1 \rangle, \langle Y_2 \rangle) \, \mathrm{d}z, \tag{3.6}$$

and is preferred for analysing the growth rate compared with (3.3) since it has the advantage of avoiding dependence on statistical fluctuations (Cook & Dimotakis 2001; Cabot & Cook 2006; Cabot & Zhou 2013). Figure 14 shows h for different ρ_2/ρ_1. In this case, a larger density ratio contributes to a larger mixing region width, consistent with the contour plots in §3.1. The behaviour of h defined in (3.6) is analysed in the next section.

3.3. *Self-similarity and scaling of the mixing region width*

The scaling of the mixing region width h with time is a quantity of practical engineering importance. With the present problem set-up, turbulent diffusion of a passive scalar, i.e. $\rho_2 = \rho_1$, is expected to be a self-similar process with the same growth rate in each z direction since the dissipation rate, and thus the turbulence, are identical in each fluid. This behaviour is confirmed for all density ratios by plotting the average mass fraction field as a function of the similarity variable $\xi = z/h$ in figure 15. As the density ratio is increased, self-similarity is still observed, though it takes longer to develop and in the most mixed regions ($0.4 \lesssim \langle Y \rangle \lesssim 0.6$) the profiles do not perfectly collapse at the higher density ratios.

We seek to determine the scaling of h with time. This mixing process can be described by one-dimensional (turbulent) diffusion of one fluid into the other:

$$\frac{\partial Y}{\partial t} = \frac{\partial}{\partial z}\left(\kappa \frac{\partial Y}{\partial z}\right), \tag{3.7}$$
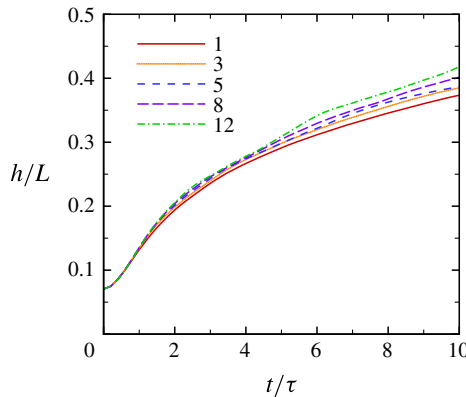
FIGURE 14. (Colour online) Temporal evolution of the mixing region width h based on (3.6) for $Re_{\lambda,o} = 100$, and different ρ_2/ρ_1.

where Y is the mass fraction and κ is an effective diffusion coefficient that varies with time and may be Reynolds-number dependent. After integrating (3.7) for $z < 0$, and rearranging following Lawrie & Dalziel (2011), we obtain

$$h\dot{h} = \kappa \left(\frac{\left. \dfrac{\partial Y}{\partial \xi} \right|_{\xi=0}}{-\displaystyle\int_{-\infty}^{0} Y(\xi)\,\mathrm{d}\xi} \right). \tag{3.8}$$

Since the expression in parentheses is a constant, $h\dot{h} \sim \kappa$. To determine κ, Prandtl's mixing length theory, $\kappa \sim u_{turb}l_{turb}$, is invoked, where $u_{turb} = u_{rms}$, $l_{turb} = \lambda$, where λ is the Taylor microscale. Since μ/ρ is the same for both fluids, $\kappa \sim Re_\lambda$. Theoretical self-preserving analysis as well as grid turbulence experiments for a decaying isotropic field (George 1992) support the following scalings:

$$\lambda \sim t^{1/2}, \quad u_{rms}^2 \sim t^{-n}. \tag{3.9a,b}$$

Thus, $Re_\lambda \sim t^{(1-n)/2}$. Defining $\alpha = (1-n)/2$, the power-law behaviour of $Re_\lambda \sim t^\alpha$ yields the following scaling for the mixing region width:

$$h \sim t^{(\alpha+1)/2} \sim t^{1-n/2}. \tag{3.10}$$

The same scaling of the mixing region with time can be obtained by other approaches (e.g. that of Layzer (1955) or simple control volume analysis), with the key assumption being that the kinetic energy decays as a power law with respect to time. We note that according to Dimotakis (2000) the turbulence is not fully developed in the self-similar regime (recall figure 1) since Re_λ falls below 100 for the major part of our simulations, such that Reynolds-number dependence is expected in this scaling. These observations are confirmed in figure 16, although the sensitivity to the Reynolds number is relatively weak. This can be explained by noticing that the difference in Re_λ is less than 25 at any time during the self-similar regime for the present initial Taylor-scale Reynolds numbers ($60 \leqslant Re_{\lambda,o} \leqslant 200$). This small change in α does not significantly affect h.
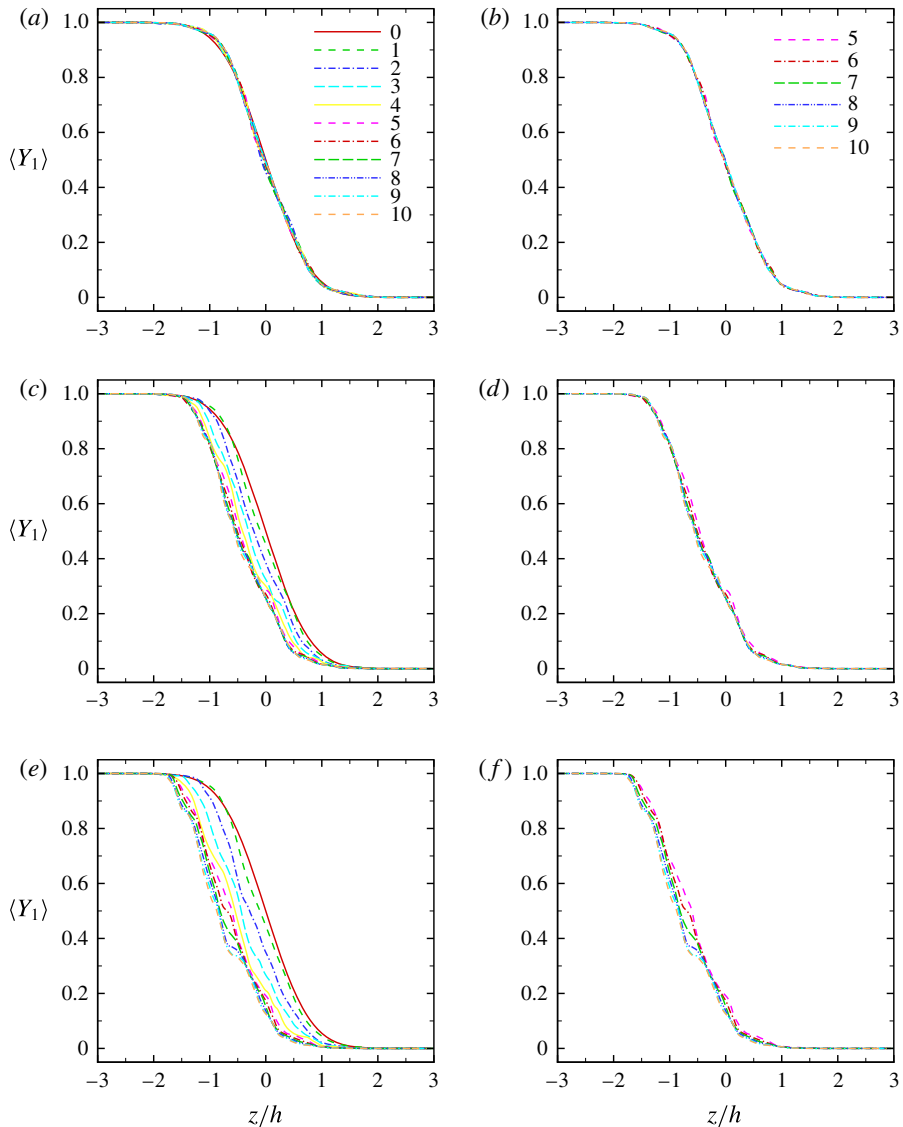
FIGURE 15. (Colour online) Average mass fraction field in the x–y plane at different times for $Re_{\lambda,o} = 100$ and $\rho_2/\rho_1 = 1$ (a,b), 5 (c,d) and 12 (e,f): (a,c,e) 0–10τ; (b,d,f): 5–10τ.

3.3.1. *High-Reynolds-number limit*

This analysis can be taken one step further by assuming fully developed turbulence, in which case we can compute the actual exponent based on energy considerations previously used for Rayleigh–Taylor turbulence near bubbles and spikes (Abarzhi, Gorobets & Sreenivasan 2005). Grid turbulence experiments of decaying homogeneous isotropic turbulence support the following empirical law (Comte-Bellot & Corrsin 1966) for the velocity fluctuations:

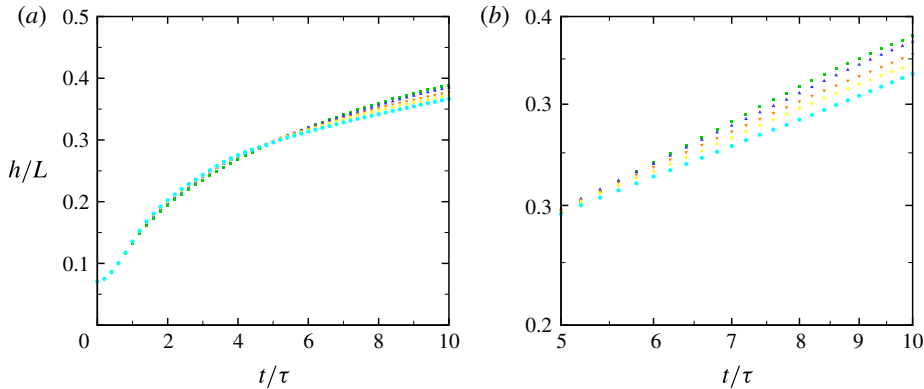$$\frac{\mathrm{d}u^2}{\mathrm{d}t} \sim -\frac{u^3}{l}, \tag{3.11}$$

FIGURE 16. (Colour online) Time evolution of the mixing region width (with $\rho_2/\rho_1 = 3$) for $Re_{\lambda,o} = 60$ (squares, green), 100 (upward-pointing triangles, blue), 120 (downward-pointing triangles, orange), 140 (diamonds, yellow) and 200 (circles, cyan): (*a*) linear–linear; (*b*) log–log.

where l is the integral scale. A fluid parcel initially at the interface is transported by eddies of different sizes in the fluctuating velocity field u. The largest eddies of size l contribute the most to the growth of the mixing region, thus suggesting a scaling $h \sim l$. This scaling is in agreement with the water tunnel grid-generated turbulence experiments of Huq & Britter (1995*a*). The dynamics of the mixing region can also be related to the fluctuating field as $\dot{h} \sim u$. For the Batchelor spectrum considered here, $u^2 l^5$ is an invariant, which corresponds to conservation of angular momentum (Batchelor & Proudman 1956). Substituting into (3.11) yields

$$u^2 \sim t^{-10/7}, \quad h \sim l \sim t^{2/7}. \tag{3.12a,b}$$

This result provides an asymptotic limit for the exponent in fully developed (Reynolds-number-independent) turbulence starting from a Batchelor spectrum.

3.3.2. *Comparison between theory and simulations*

The above arguments can be verified by comparing $h(t)$ computed directly from the DNS with that obtained by measuring α from $Re_\lambda(t)$ and substituting into (3.10). A power-law least-squares fit to Re_λ in the mixing region is performed to find α at different $Re_{\lambda,o}$. To compute h, we use the regression method of Krogstad & Davidson (2010). The process relies on a linear best fit for

$$\ln h = \ln(a) + n \ln(t - t_0), \tag{3.13}$$

where t_0 is the virtual point of origin. Assuming that d_i is the fitted function, for each t_0 the variance can be defined as

$$\sigma^2 = \frac{1}{N-1} \sum_{i=1}^{N} [d_i(x_i) - h(x_i)]^2. \tag{3.14}$$

We consider $t_0/\tau = 0.0$, 0.5, 1.0, 1.5 and 2.0. Since $t_0/\tau = 0.0$ and 0.5 yield the smallest σ^2, we report data corresponding to these two values. As described in §2.3,

t_0/τ		$Re_{\lambda,o} = 60$	$Re_{\lambda,o} = 100$	$Re_{\lambda,o} = 120$	$Re_{\lambda,o} = 140$	$Re_{\lambda,o} = 200$
0.0	α	-0.420	-0.377	-0.371	-0.371	-0.326
	Predicted growth	0.290	0.311	0.314	0.314	0.337
	Observed growth	0.383	0.358	0.349	0.327	0.316
	Error	24.2 %	13.1 %	10.0 %	4.0 %	-6.6 %
0.5	α	-0.386	-0.350	-0.345	-0.345	-0.304
	Predicted growth	0.307	0.325	0.327	0.327	0.348
	Observed growth	0.352	0.333	0.324	0.304	0.293
	Error	12.8 %	2.4 %	-0.9 %	-7.5 %	-18.8 %

TABLE 2. Scaling of h with time for $\rho_2/\rho_1 = 1$, and virtual origins $t_0/\tau = 0.0$ and 0.5. The predicted growth $(\alpha + 1)/2$ is obtained using (3.10) by fitting $Re_\lambda \sim t^\alpha$. The observed growth is calculated by performing a direct data fit to h. The same interval $(5–10\tau)$ is used in each case to obtain α and the observed growth. The error is defined as (observed growth – predicted growth)/observed growth.

it takes approximately 2τ for the initial field to evolve to turbulence; additional time is expected to be required for the mass fraction field to become correlated with the velocity field and result in self-similar growth, as supported by figure 15 in which the data collapses well between 5 and 10τ. Thus, we pick $t = 5\tau$ as a safe choice for the beginning of the self-similar regime in our analysis and take $t = 10\tau$ as the final time to prevent box-size effects. The growth obtained using the two different approaches (directly from the DNS versus computing α from Re_λ) is compared in table 2 for $\rho_1/\rho_2 = 1$ and table 3 for $\rho_1/\rho_2 = 3$, and figure 17 shows the exponent of time for different $Re_{\lambda,o}$ and density ratios. The exponents lie in the range 0.29–0.38 for a density ratio of 1 and 0.28–0.39 for a density ratio of 3; overall, the agreement between the two different approaches for measuring the time exponent is good. The general trend shows that the growth exponent decreases as $Re_{\lambda,o}$ increases, and in fact tends to the asymptotic limit of fully developed turbulence (3.12). The discrepancy in the growth exponent decreases as $Re_{\lambda,o}$ increases up to 140. The decrease in the growth of the mixing region likely is related to the higher enstrophy (i.e. dissipation) at higher $Re_{\lambda,o}$ during the self-similar regime. Figure 17 suggests that the growth exponent, and thus mixing region width, increases with the density ratio for a given $Re_{\lambda,o}$, but this dependence is not completely monotonic. As discussed in § 3.2, for a density ratio of one, the mixing region grows symmetrically in both fluids. At higher density ratios, the mixing region grows asymmetrically as an eddy in the heavy fluid has higher momentum than the corresponding volume of light fluid, such that it is easier for the heavy fluid to displace the light fluid and penetrate it. By the same argument, it is more difficult for the light fluid to penetrate the heavy fluid.

The Batchelor spectrum is commonly used to initialise this problem in numerical simulations and is thus the focus of the present work. Nevertheless, the analysis for fully developed turbulence holds for other spectra, e.g. Saffman's, $E(k) \sim k^2$, in which case $u^2 l^3$ is the relevant flow invariant (Saffman 1967). Starting from (3.11), a Saffman spectrum yields $h \sim l \sim t^{2/5}$. For $Re_{\lambda,o} = 60$, 100, 140 and 200 and a virtual origin of $t_0 = 0$, passive scalar simulations ($\rho_2/\rho_1 = 1$) produce time exponents 0.44, 0.43, 0.39 and 0.37, respectively. Again, similar trends are observed, though the asymptotic limit slightly undershoots the prediction. We note that box-size effects become important earlier due to a more rapid growth with a Saffman spectrum and may thus reduce the computed exponent.
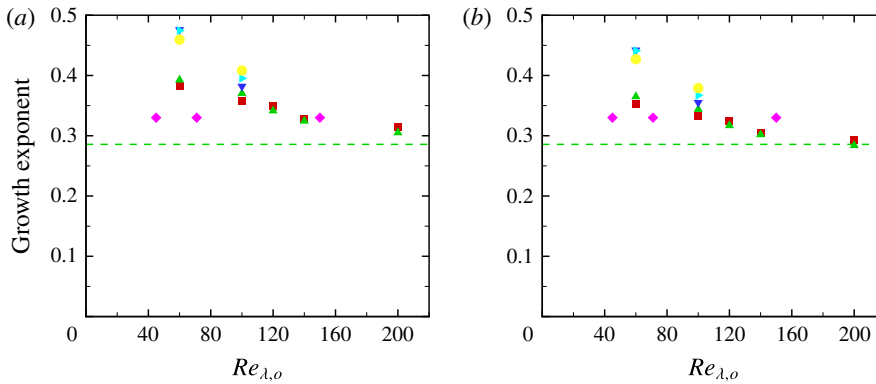
FIGURE 17. (Colour online) Time exponent of the mixing region width computed directly from the DNS: $\rho_2/\rho_1 = 1$ (squares, red), 3 (upward-pointing triangles, green), 5 (downward-pointing triangles, blue), 8 (rightward-pointing triangles, cyan) and 12 (circles, yellow): (a) $t_0/\tau = 0.0$; (b) $t_0/\tau = 0.5$. Purple diamonds: DNS of Tordella & Iovieno (2011). Green dashed line: theoretical growth exponent of $2/7$ (3.12).

t_0/τ		$Re_{\lambda,o} = 60$	$Re_{\lambda,o} = 100$	$Re_{\lambda,o} = 120$	$Re_{\lambda,o} = 140$	$Re_{\lambda,o} = 200$
0.0	α	-0.409	-0.360	-0.341	-0.353	-0.339
	Predicted growth	0.295	0.320	0.329	0.323	0.330
	Observed growth	0.393	0.370	0.342	0.325	0.306
	Error	24.9 %	13.5 %	3.8 %	0.6 %	-7.8 %
0.5	α	-0.379	-0.334	-0.317	-0.328	-0.315
	Predicted growth	0.310	0.333	0.341	0.336	0.342
	Observed growth	0.365	0.344	0.317	0.302	0.284
	Error	15.0 %	3.2 %	-7.6 %	-11.3 %	-20.4 %

TABLE 3. Scaling of h with time for $\rho_2/\rho_1 = 3$, and virtual origins $t_0/\tau = 0.0$ and 0.5. The predicted growth $(\alpha + 1)/2$ is obtained using (3.10) by fitting $Re_\lambda \sim t^\alpha$. The observed growth is calculated by performing a direct data fit to h. The same interval $(5–10\tau)$ is used in each case to obtain α and the observed growth. The error is defined as (observed growth – predicted growth)/observed growth.

Our predicted values are consistent with past results, both experimental and computational. DNS of passive scalar mixing (Tordella & Iovieno 2011), in which isotropic turbulent fields with the same Taylor scale but different kinetic energy are juxtaposed, obtained a scaling $h \sim t^{0.33}$ based on multiple simulations with $Re_\lambda = 45–150$ after the initial transient (Tordella & Iovieno 2011, figure 1). Our set-up is different, since the turbulent fields used here have the same volume-averaged kinetic energy per unit mass $u_{rms}^2/2$ but different kinetic energy per unit volume $\rho u_{rms}^2/2$, which enables us to isolate the effect of the density gradient and investigate level 2 mixing. A k–ϵ turbulent diffusion model (Anand & Pope 1983) was used to predict a $t^{0.34}$ growth for experimental wind tunnels studies of the development of a thermal wake in an isotropic grid-generated turbulence behind a heated wire (Warhaft 1984; Stapountzis *et al.* 1986) at the last stage of the development of the thermal wake (turbulent diffusive stage). While the model of Anand & Pope (1983) fits the experimental data well, the slope of a power-law fit to the mixing region width does

not reach the predicted growth. The observed time exponent for the growth of the mixing region in this study is close to those reported in studies of turbulent mixing following the Richtmyer–Meshkov instability after reshock (Tritschler *et al.* 2014). This observation is expected, since the turbulence produced by such flows is very similar to that in the present study.

3.3.3. *Effect of k_o*

The ratio of the initial Taylor microscale ($\lambda_o = 2/k_o$) to the domain size L is yet another parameter that enters the problem. In practice, $k_o = 4$ is commonly used in studies of isotropic turbulence (Lee *et al.* 1991; Larsson & Lele 2009; Johnsen *et al.* 2010; Bhagatwala & Lele 2011, 2012). A higher k_o is desirable to reduce box-size effects, as is sometimes done in Rayleigh–Taylor turbulence (Cabot & Cook 2006). In addition, putting the initial energy at higher modes allows for a more natural transition to a fully developed state from the initial artificial spectrum, specifically with regard to achieving a spectrum $E(k) \sim k^4$ at low wavenumbers. On the other hand, increasing k_o significantly increases the required grid resolution. We performed most of our simulations with $k_0 = 4$ to resolve all scales on a grid of $N = 256$ per L. Here, we discuss the sensitivity of the results on k_o by considering the passive scalar case ($\rho_2 = \rho_1$) with $k_0 = 8$ and $Re_{\lambda,o} = 60$–140 on a grid of $N = 512$ per L. We set the initial thickness of the diffuse interface to be half that used for k_o by doubling H in (2.17), such that the ratio of λ_o to the initial mixing thickness is the same as for $k_o = 4$. A corresponding self-similar behaviour is also observed for $k_o = 8$, with time exponents 0.335, 0.328 and 0.323 corresponding to $Re_{\lambda,o} = 60$, 100 and 140, respectively. As for $k_o = 4$, the exponents decrease with increasing $Re_{\lambda,o}$, although at a reduced rate. Compared with the $k_o = 4$ results, the mixing region width at 10τ is half. Furthermore, the self-similar behaviour is observed up to 20τ for $k_o = 8$, after which point box-size effects become evident. Thus, if one is interested in studying the problem until times later than 10τ, higher values of k_o should be considered to prevent box-size effects, although the computational cost is higher. The current data fit for $k_0 = 4$ is performed on the interval $5\tau < t < 10\tau$ to avoid box-size effects and to remain in the self-similar regime. A longer period of self-similar behaviour in time compared with the current work would be desirable for a power-law fit.

3.4. *Mixedness*

Mixing can be quantified by considering a hypothetical reaction between two pure fluids where the fully mixed fluid is the product corresponding to a stoichiometric mixture of the two fluids (Cook & Dimotakis 2001). We use mass fraction for convenience instead of volume fraction typically used in the incompressible case. The mass fraction of the mixed fluid is

$$Y_m(Y) = \begin{cases} 2Y & \text{if } Y \leqslant 0.5, \\ 2(1 - Y) & \text{if } Y > 0.5, \end{cases} \tag{3.15}$$

where the stoichiometric coefficient is taken to be 0.5. The mixing region width (entrainment length) is defined as

$$h_m = \int_{-\infty}^{\infty} Y_m(\langle Y \rangle) \, \mathrm{d}z, \tag{3.16}$$
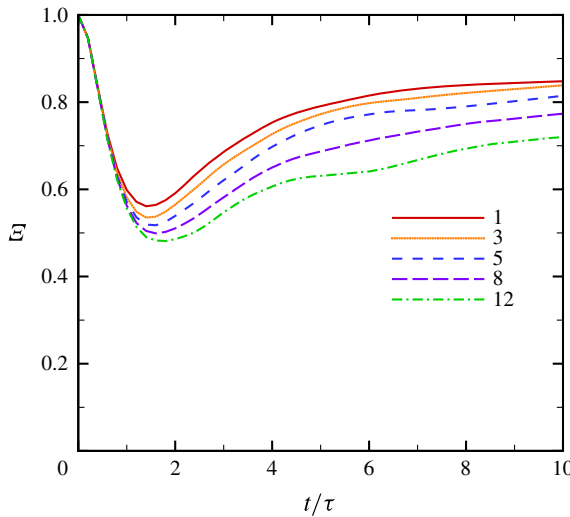
FIGURE 18. (Colour online) Temporal evolution of the mixedness Ξ for $Re_{\lambda,o} = 100$ and different density ratios.

where h_m represents the maximum thickness of the product fluid (mixed fluid) if the fluid entrained into the mixing region is perfectly mixed in each x–y plane, thus implying that there are no perturbations from the mean. For a stoichiometric coefficient of 0.5, (3.16) reduces to (3.6). A measure of mixedness, Ξ, can be defined by comparing the total amount of the product with the maximum possible product as

$$\Xi = \frac{\int_{-\infty}^{\infty} \langle Y_m \rangle \, dz}{h_m}. \tag{3.17}$$

Figure 18 shows the temporal evolution of the mixedness in the mixing region. Since no perturbation exists in each x–y plane initially, Ξ starts from unity and decreases as the velocity field perturbs the mass fraction and entrains one fluid into the other, thus creating inhomogeneous regions in x–y. After this transition period, the mass fraction perturbations in x–y decrease. This behaviour is due to the decay in the velocity and enstrophy fields, such that the fluid newly entrained into the mixing region is not sufficiently energetic to perturb the mass fraction field. At later times, the variation in Ξ decreases, thus suggesting a balance between molecular diffusion and entrainment from the 'edges' of the mixing region. With increasing density ratio, the mixedness decreases owing to the larger density and mass fraction fluctuations. On the other hand, the mixing region width increases because the heavier fluid has higher momentum (recall figure 14). These observations are consistent with the qualitative features of figures 8 and 9.

4. Results: dynamics of the small scales in the mixing region

We now shift our focus to the small scales. To quantify flow isotropy across the different turbulent scales in the mixing region, energy spectra are first considered in § 4.1. Then anisotropy at different length scales is investigated (§ 4.2), followed by an examination of intermittency in § 4.4. All of the quantities reported in this section are measured well within the mixing zone, in the range $0.25 \leqslant \langle Y \rangle \leqslant 0.75$.

4.1. *Two-dimensional energy spectra*

To better understand the energy distribution in the mixing region, the cumulative energy spectra, defined as

$$C_\phi(k) = \frac{\displaystyle\int_0^k E_\phi(k')\,\mathrm{d}k'}{\displaystyle\int_0^\infty E_\phi(k')\,\mathrm{d}k'}, \tag{4.1}$$

are considered (Mueschke & Schilling 2009). This quantity measures how the energy is distributed between wavenumbers 0–k, where k is the magnitude of the two-dimensional wavevector $\boldsymbol{k}$ in the x–y plane. At each x–y plane in the mixing region, the two-dimensional energy spectra for each fluctuating field $\phi' = \phi - \langle\phi\rangle$ are calculated and averaged in the z direction inside the mixing region. Figure 19 shows C_ϕ for the velocity, mass fraction and density fluctuating fields. Since the initial density and mass fraction fields do not contain any perturbations in the x–y planes, $C = 1$ initially for these quantities. As turbulence starts to develop from the initial random field, energy gets transferred to higher wavenumbers. After the initial transition time (up to 2–4τ), the relative distribution of energy between different modes reverses as the turbulence decays.

To determine the effect of the density ratio on the different scales, spectra of density, mass fraction and velocity fluctuations are shown in figure 20 for different density ratios at $Re_{\lambda,o} = 100$ and $t = 5\tau$, i.e. during self-similar growth. Increasing the density ratio does not have a significant effect on the mass fraction spectra, but yields larger energy contents at low wavenumbers in the density and z-velocity spectra. The dependence of the z-velocity spectra on the density ratio is attributable to varying background pressures (2.18); the larger density ratios yield higher density fluctuations across all scales at a given time.

4.2. *Temporal evolution of the Taylor and Kolmogorov scales*

Perhaps the clearest indicator of anisotropy is one based on the calculation of directional length scales in the mixing region, namely Taylor and Kolmogorov scales, λ_i and η_i, respectively, in the ith direction (Cook & Dimotakis 2001; Cabot & Zhou 2013):

$$\lambda_i(z,t) = \left[\frac{\langle u_i^2\rangle}{\left\langle\left(\dfrac{\partial u_i}{\partial x_i}\right)^2\right\rangle}\right]_{mz}^{1/2}, \quad \eta_i(z,t) = \left[\frac{(\nu/Re)^3}{\epsilon_i}\right]_{mz}^{1/4}, \tag{4.2a,b}$$

where

$$\epsilon_i(z,t) = \frac{15\nu}{Re}\left\langle\left(\frac{\partial u_i}{\partial x_i}\right)^2\right\rangle \tag{4.3}$$

is the directional dissipation rate and $[\cdot]_{mz}$ is the average in the z direction well within the mixing zone, in the range $0.25 \leqslant \langle Y\rangle \leqslant 0.75$. In (4.2) and (4.3), there is no sum in i. By contrast, the overall dissipation is defined

$$\epsilon = \frac{2\nu}{Re}S_{ij}^* S_{ij}^*, \tag{4.4}$$
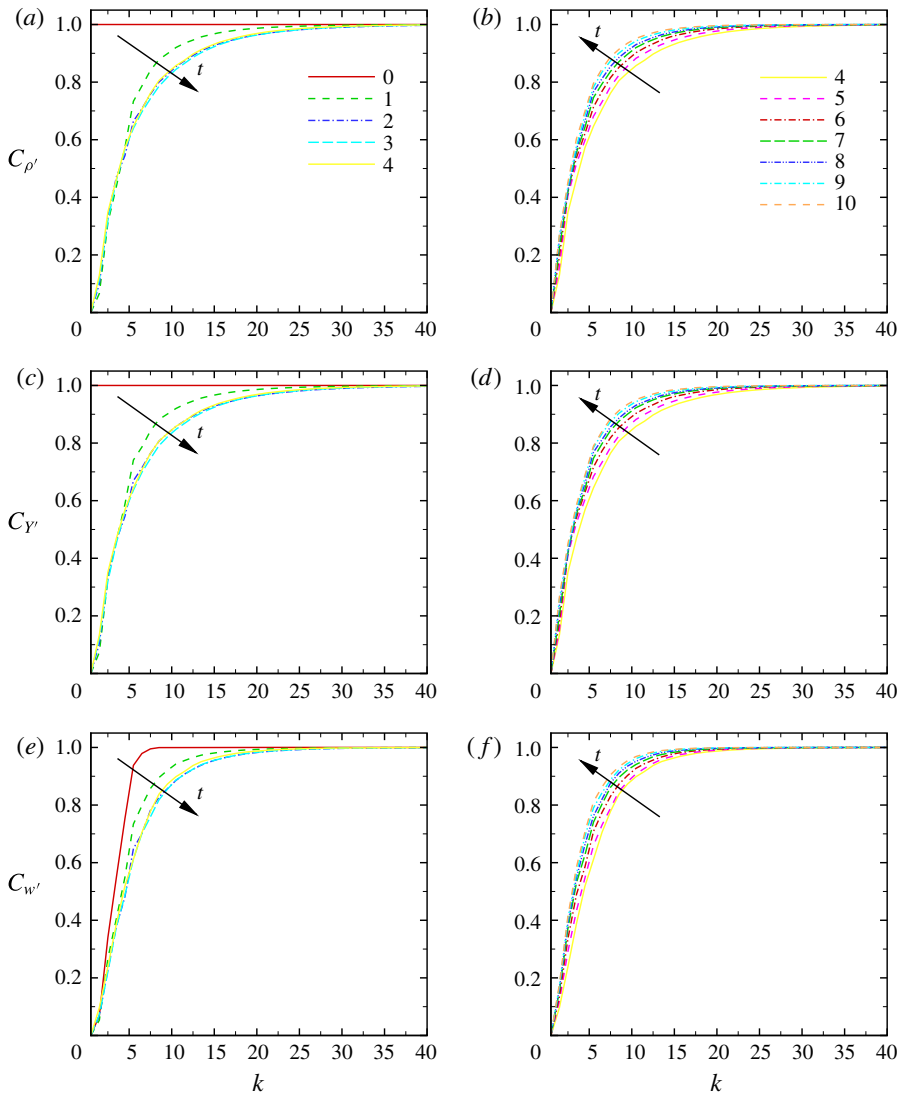
FIGURE 19. (Colour online) Cumulative energy spectra of density, mass fraction, and the z-velocity fluctuation fields at different times for $Re_{\lambda,o} = 100$ and $\rho_2/\rho_1 = 3$.

where S_{ij}^* is defined in (3.2). Equation (4.3) is commonly used in experiments to measure dissipation as it requires measuring only one of the components of the velocity gradient tensor. This definition could raise concerns regarding the accuracy of dissipation measurements, especially in anisotropic fields (Sreenivasan & Antonia 1997) since (4.3) corresponds to (4.4), the exact definition of dissipation, only for spherical symmetry in incompressible homogeneous isotropic turbulence. However, this surrogacy issue is not problematic here as (4.3) is used solely to measure isotropy at the Kolmogorov scale; the full dissipation is calculated as well.

Figure 21 shows the time evolution of the directional Taylor and Kolmogorov scales. During the initial transition period (up to approximately 2–4τ), the initial energy at large scales gets transferred to the small scales as discussed in the previous
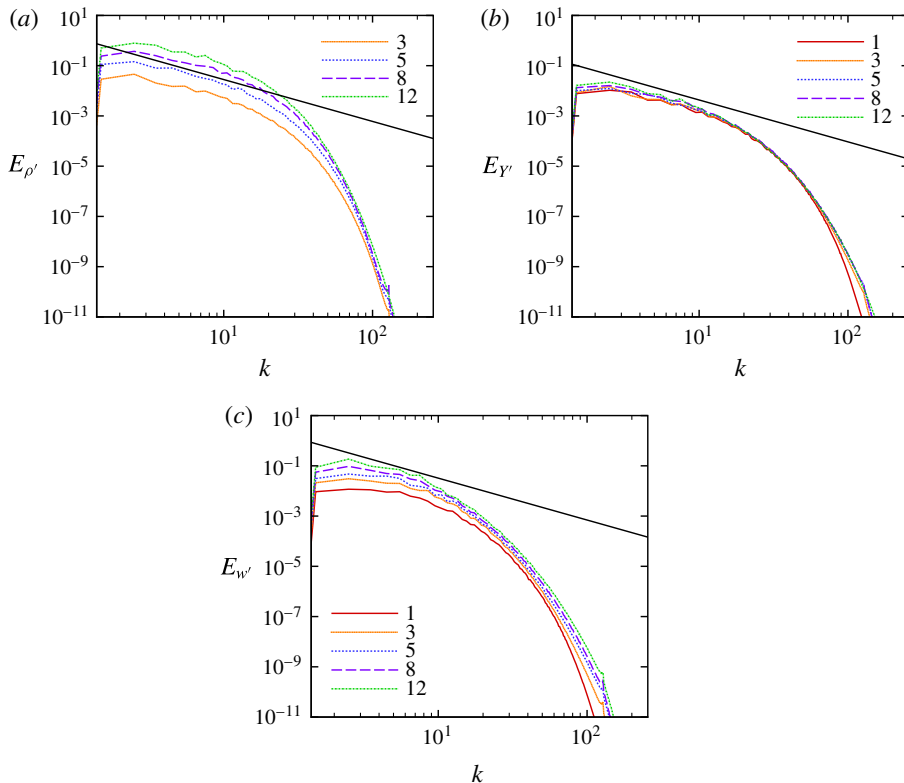
FIGURE 20. (Colour online) Two-dimensional spectra of density, mass fraction and *z*-velocity fluctuations for $Re_{\lambda,o} = 100$, $t/\tau = 5$, and $\rho_2/\rho_1 = 1$ (full curve, red), 3 (dotted, orange), 5 (short dashed, blue), 8 (long dashed, purple) and 12 (dot-dashed, green). The black line corresponds to a $-5/3$ slope.

section. This energy transfer results in an increase in enstrophy and dissipation, and consequently a decrease in the Taylor and Kolmogorov scales. After the initial transition, the developed turbulent field decays freely, and these length scales increase with time as the smallest scales dissipate the soonest (Pope 2000). The general trend in the evolution of the Taylor and Kolmogorov scales are in agreement with grid turbulence experiments and DNS of single-fluid decaying isotropic turbulence.

At a modest density ratio ($\rho_2/\rho_1 = 3$), the directional Taylor scales do not exhibit significant anisotropy. However, as the density ratio increases, the Taylor scale in the *z* direction takes higher values relative to the *x* and *y* directions, representing anisotropy at that scale in the *z* direction. This anisotropy also increases with time. As described in § 3.2, the density field evolves with the velocity during the initial transient, after which the effect of the density gradient becomes more pronounced through turbulent diffusion, as explained in § 3.3. The fact that the flow is nearly isotropic at the Taylor scale for $\rho_2/\rho_1 = 3$ is particularly important in terms of Rayleigh–Taylor turbulence as many DNS are performed at this density ratio (Cook & Dimotakis 2001; Cabot & Cook 2006); typically the anisotropy in the composition/density is considered as one of the main sources of anisotropy in addition to gravity in these flows. At the smallest scales, the turbulence is isotropic despite the large-scale anisotropy in density, as all
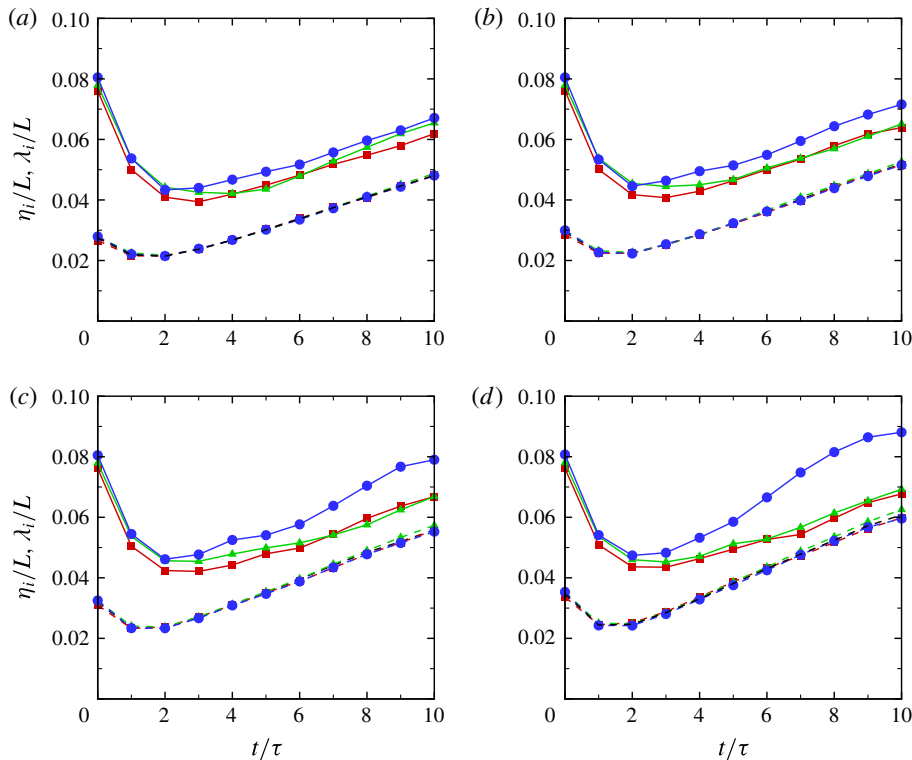
FIGURE 21. (Colour online) Time evolution of the directional Taylor (solid) and Kolmogorov (dashed) scales (solid) for $Re_{\lambda,o} = 100$, $\rho_2/\rho_1 = 3$ (*a*), 5 (*b*), 8 (*c*) and 12 (*d*): red squares, x component; green triangles, y component; blue circles, z component. The Kolmogorov scale used by measuring the full dissipation is also plotted in black.

three curves essentially fall onto each other. In other words, the average dissipation rate is the same in each direction, as expected for an isotropic field.

At the small scales, the growth rate of η_i is essentially the same for all density ratios, thus suggesting that small scales are dissipated at a similar rate. This result is expected since the initial Taylor-scale Reynolds number and dissipation rate are the same across the entire field for all density ratios. The minimum achieved increases slightly with density ratio. Although both sets of length scales increase with time, the growth rate of η_i is slightly higher than that of λ_x and λ_y as the density ratio is increased.

Anisotropy of the flow field can be investigated by considering the anisotropy tensor, defined as

$$B_{ij} = \left[\frac{\langle u_i u_j \rangle}{2E} - \frac{1}{3}\delta_{ij} \right]_{mz}, \tag{4.5}$$

where E is the turbulent kinetic energy per unit mass and $\langle u_i u_j \rangle$ is the ij component of the Reynolds stress tensor. For an isotropic field, $B_{ii} = 0$ since $\langle u^2 \rangle = \langle v^2 \rangle = \langle w^2 \rangle$. For Rayleigh–Taylor turbulence, $B_{11} \approx B_{22} \approx -1/6$ and $B_{33} \approx 1/3$ as $\langle u^2 \rangle \approx \langle v^2 \rangle \approx \langle w^2 \rangle/4$ (Pope 2000; Ramaprabhu, Karkhanis & Lawrie 2013). Figure 22 shows the temporal evolution of different components of the anisotropy tensor for various density ratios. For a density ratio of 3, the three measured components of the tensor remain close
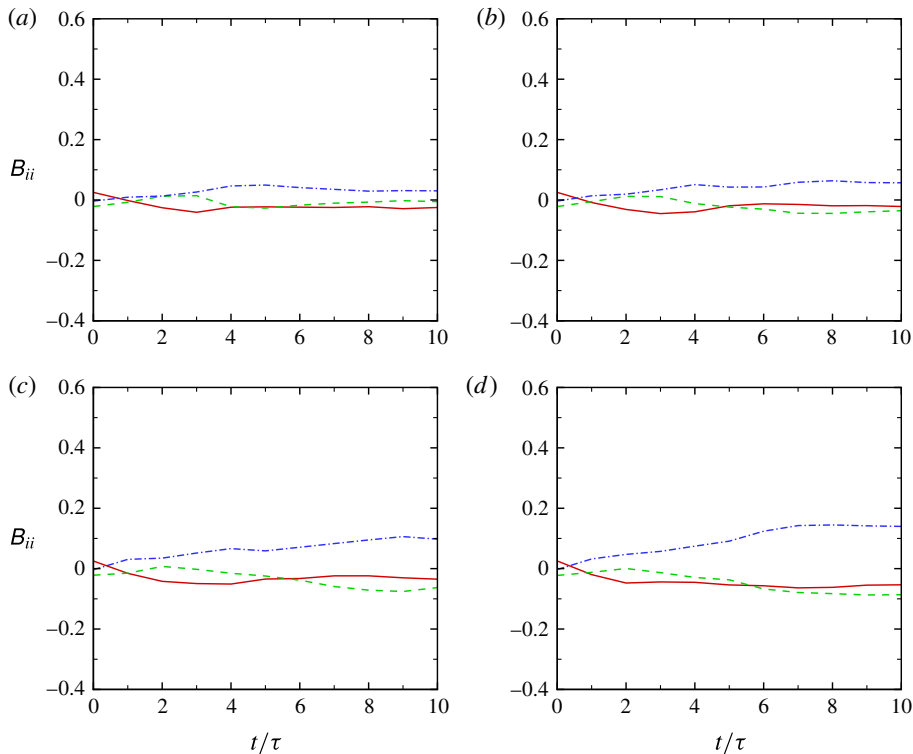
FIGURE 22. (Colour online) Time evolution of the anisotropy tensor for $Re_{\lambda,o} = 100$, $\rho_2/\rho_1 = 3$ (*a*), 5 (*b*), 8 (*c*) and 12 (*d*): solid, red, *x* component; dashed, green, *y* component; dot-dashed, blue, *z* component.

to zero, corresponding to an isotropic field. As the density ratio increases, B_{33} also increases, while B_{11} and B_{22} decrease slightly. For a density ratio of 12, B_{33} reaches a high value of 0.17 at late times, representing large-scale anisotropy by the current measure. This behaviour is in agreement with the large-scale anisotropy observed for the directional Taylor microscale in the direction of the initial large-scale anisotropy.

After investigating the temporal evolution of the anisotropy tensor, we focus on how the velocity derivative tensor behaves across different scales at a given time. The velocity field is first coarse-grained by applying a spatial low-pass box filter over a sphere of radius *r* (Tao, Katz & Meneveau 2002). The enstrophy corresponding to the coarse-grained velocity is expected to scale as $r^{4/3}$ for *r* within the inertial range (Pope 2000). Figure 23 shows the enstrophy and the compensated enstrophy of the coarse-grained velocity at $t/\tau = 5$ for different density ratios. The enstrophy is expected to decrease as *r* increases for isotropic turbulence. This behaviour is observed for density ratios up to 8, but for the enstrophy with a density ratio of 12 exhibits non-monotone behaviour at smaller values of *r*. The compensated enstrophy plots show a clear inertial range in which $\langle \omega_i \omega_i \rangle \sim r^{4/3}$, for density ratios up to 5. The width of the inertial range decreases significantly for a density ratio of 8, while we do not observe any inertial range for the density ratio of 12. It is interesting to note that for small *r* the coarse-grained enstrophy converges to the isotropic case (density ratio of 1) and does not exhibit significant dependence on the density ratio. As *r* and density ratio increase, the coarse-grained enstrophy departs from the isotropic case. Naso & Pumir
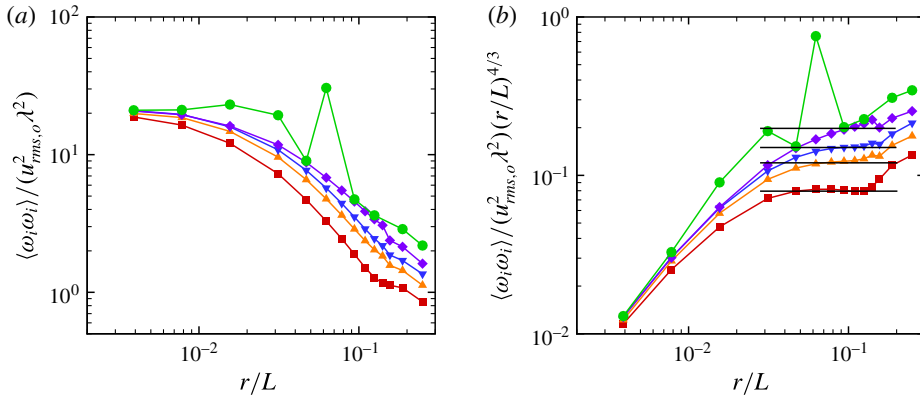
FIGURE 23. (Colour online) Scaling of the coarse-grained enstrophy (*a*) and compensated enstrophy (*b*) for $Re_{\lambda,o} = 100$, $t/\tau = 5$, and $\rho_2/\rho_1 = 1$ (squares, red), 3 (upward-pointing triangles, orange), 5 (downward-pointing triangles, blue), 8 (diamonds, purple) and 12 (circles, green).

(2005) reported a similar departure from the isotropic case in the context of shear flows by changing the mean shear (Naso, Pumir & Chertkov 2006; Eyink & Aluie 2009).

4.3. *Temporal evolution of the relevant length scales in the mass fraction field*

Similar ideas can be used to examine isotropy in the mass fraction field. The directional Corrsin scale is given by (Monin & Yaglom 1975; Antonia *et al.* 2013):

$$\lambda_i^Y = \left[\frac{\langle Y'^2 \rangle}{\left\langle \left(\frac{\partial Y'}{\partial x_i} \right)^2 \right\rangle} \right]_{mz}^{1/2}, \tag{4.6}$$

and the directional turbulent 'scalar' dissipation is defined as

$$\chi_i = \left[\frac{6}{Re\,Sc} \left\langle \left(\frac{\partial Y'}{\partial x_i} \right)^2 \right\rangle \right]_{mz}. \tag{4.7}$$

Based on dimensional arguments, the corresponding directional dissipation length scale is $\eta_i^Y \sim (Re\,Sc)^{-3/4} \chi_i^{-1/4}$. These quantities are shown in figures 24 and 25, along with the mass fraction fluctuations in figure 26. By contrast to the length scales relevant to the velocity field, the current results suggest that for a fixed density ratio the mass fraction field remains isotropic from the dissipation scale to the Corrsin scale, except small deviations at late times. Given that the Corrsin microscale represents the large-scale mass fraction fluctuations, higher values are observed as both the mass fraction fluctuations and the mixing region width are larger at higher density ratios. This phenomenon can be explained by the higher mass fraction fluctuations at higher density ratios, which lead to higher dissipation rates. The Corrsin scale is 10 times smaller than the Taylor microscale of the velocity field, which suggests that resolution requirements to resolve the Corrsin microscale accurately are much higher than those for the Taylor microscale.
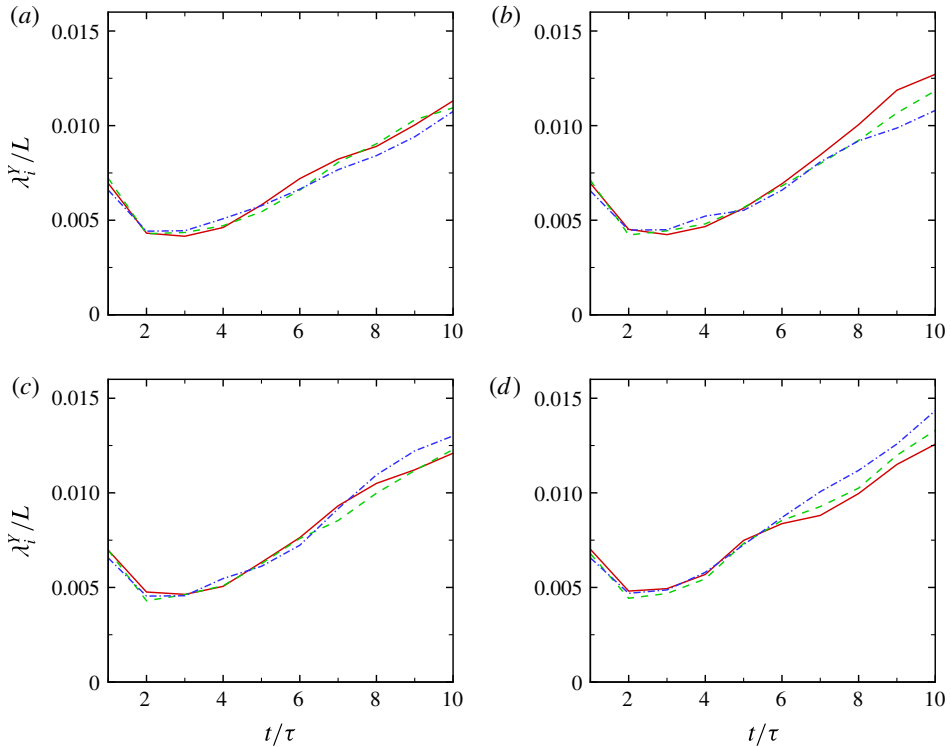
FIGURE 24. (Colour online) Time evolution of the directional Corrsin microscale for $Re_{\lambda,o} = 100$, and $\rho_2/\rho_1 = 3$ (*a*), 5 (*b*), 8 (*c*) and 12 (*d*): solid, red, *x* component; dashed, green, *y* component; dot-dashed, blue, *z* component.

4.4. *Flow intermittency*

Small-scale intermittency of the velocity field is considered by measuring the directional skewness *S* and kurtosis *K* of the velocity derivatives in the mixing region ($0.25 \leqslant \langle Y \rangle \leqslant 0.75$), also measured in Tordella *et al.* (2008) and Cabot & Zhou (2013). These quantities are defined as

$$S_{(\partial u_i/\partial x_i)} = \left[\frac{\left\langle \left(\dfrac{\partial u_i}{\partial x_i} \right)^3 \right\rangle}{\left\langle \left(\dfrac{\partial u_i}{\partial x_i} \right)^2 \right\rangle^{1.5}} \right]_{mz} , \quad K_{(\partial u_i/\partial x_i)} = \left[\frac{\left\langle \left(\dfrac{\partial u_i}{\partial x_i} \right)^4 \right\rangle}{\left\langle \left(\dfrac{\partial u_i}{\partial x_i} \right)^2 \right\rangle^2} \right]_{mz} , \qquad (4.8a,b)$$

where there is no sum in *i*. Despite the different density ratios, the skewness of the velocity derivatives remains at the same level ($S \approx -0.5$) in all directions despite the different density ratios (figure 27), corresponding to past grid turbulence experiments (Sreenivasan & Antonia 1997); the same behaviour is observed in the kurtosis (figure 28) and suggests that the higher derivatives of the velocity field also remain isotropic. This result lies in contrast to level 1 mixing simulations with a jump in kinetic energy, which produce anisotropy in the skewness of the velocity derivatives (Tordella & Iovieno 2011). Results from our simulations and past studies indicate that
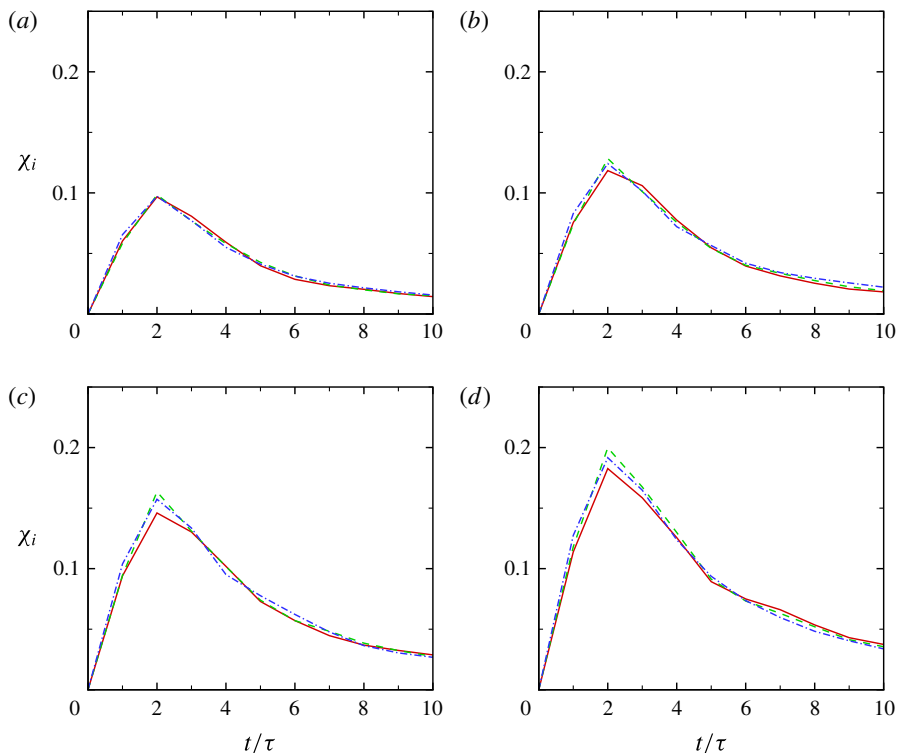
FIGURE 25. (Colour online) Time evolution of the directional turbulent scalar dissipation as defined in (4.7) for $Re_{\lambda,o} = 100$, and $\rho_2/\rho_1 = 3$ (*a*), 5 (*b*), 8 (*c*) and 12 (*d*): solid, red, x component; dashed, green, y-component; dot-dashed, blue, z component.
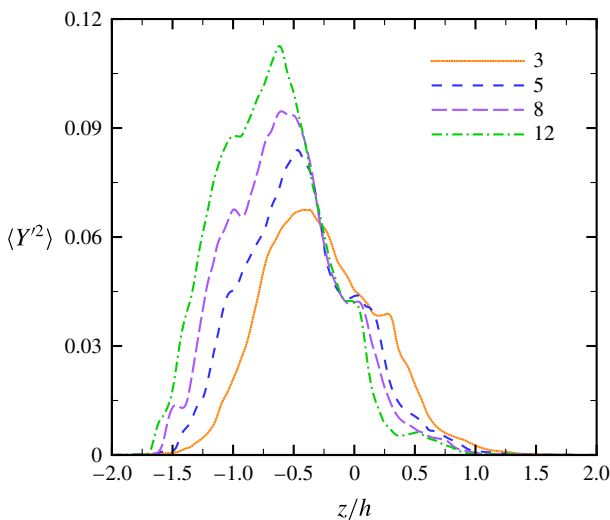

FIGURE 26. (Colour online) Average scalar fluctuation field in the x–y plane at $t/\tau = 5$ for $Re_{\lambda,o} = 100$, and $\rho_2/\rho_1 = 3$, 5, 8 and 12.
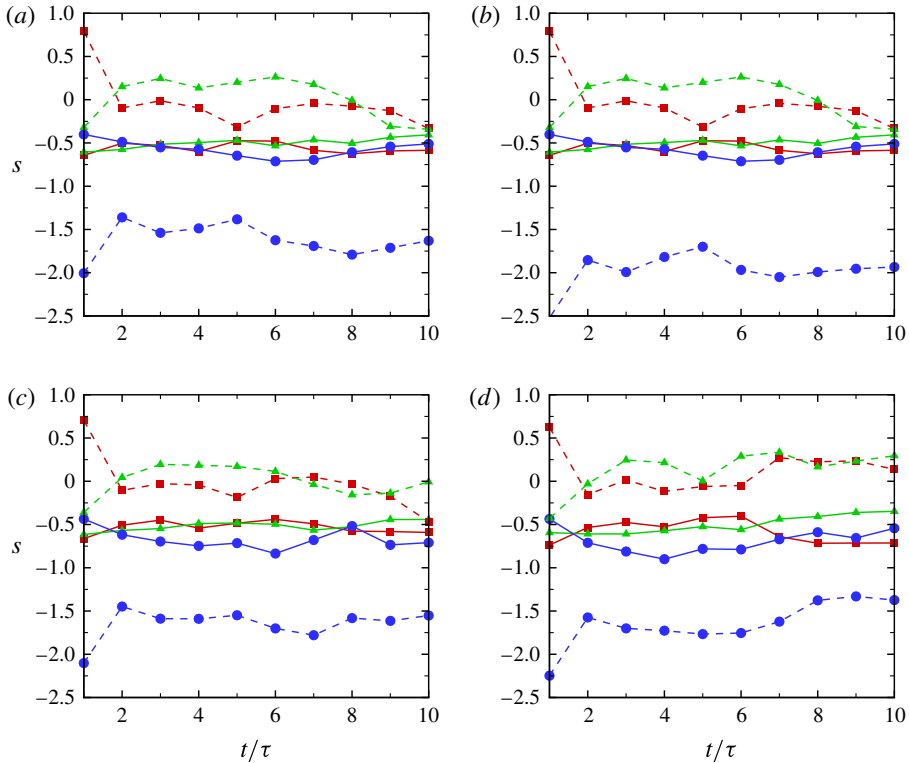
FIGURE 27. (Colour online) Time evolution of skewness of the velocity derivatives (solid) and the mass fraction derivatives (dashed) for $Re_{\lambda,o} = 100$ and $\rho_2/\rho_1 = 3$ (*a*), 5 (*b*), 8 (*c*) and 12 (*d*); red squares, *x* component; green triangles, *y* component; blue circles, *z* component.

the small-scale intermittency depends on the turbulence dynamics. Figures 27 and 28 indicates that the mass fraction field is more intermittent than the velocity field based on the higher values of the kurtosis and the higher negative value of the skewness of the mass fraction in the direction of the anisotropy. These results are consistent with grid experiments of Tong & Warhaft (1994), in which the temperature is found more intermittent than the velocity field, with a value of -1.8 ± 0.2 for the skewness of the (passive) temperature fluctuations derivative in the direction of the mean gradient.

5. Conclusions

DNS is conducted using a novel set-up to investigate level 2 turbulent mixing, with a focus on anisotropy generated solely by a density gradient. The velocity is initialised by a random solenoidal field that produces homogeneous isotropic turbulence with zero mean velocity, which is then left to decay freely in the absence of kinetic energy production mechanisms, e.g. shear in the Kelvin–Helmholtz instability or gravity in the Rayleigh–Taylor instability. Superposed onto this velocity field, an unperturbed interface initially separates a heavy fluid from a light one. The fluid properties are selected such that the kinematic viscosity, and thus the dissipation rate, is the same in both fluids despite their different densities. The rationale behind this strategy is that conventional turbulence scalings are based on kinetic energy per unit mass and
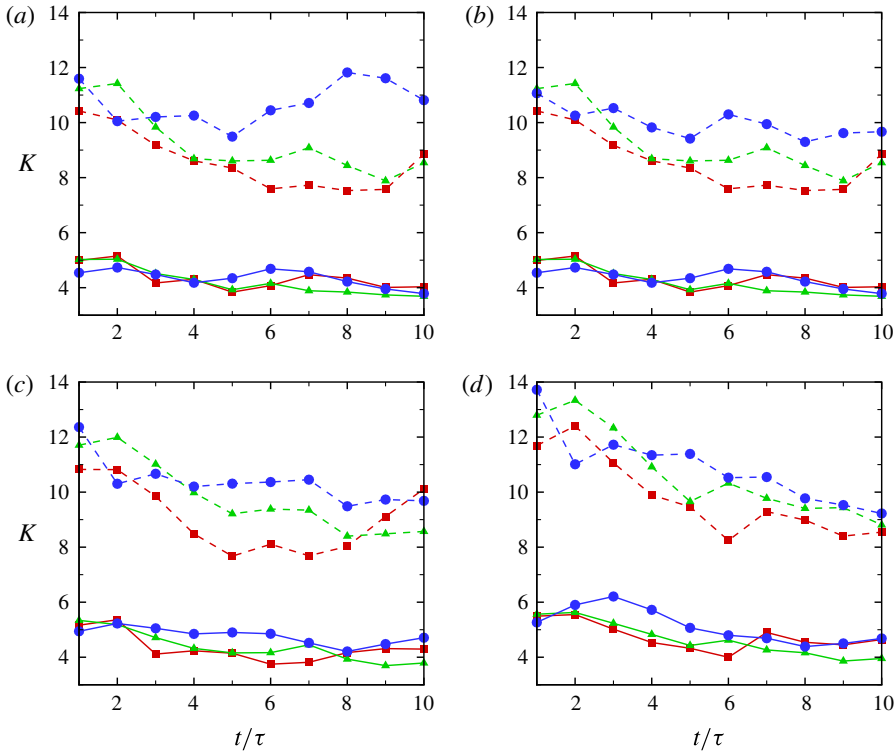
FIGURE 28. (Colour online) Time evolution of kurtosis of the velocity derivatives (solid) and the mass fraction derivatives (dashed) for $Re_{\lambda,o} = 100$ and $\rho_2/\rho_1 = 3$ (*a*), 5 (*b*), 8 (*c*) and 12 (*d*): red squares, *x* component; green triangles, *y* component; blue circles, *z* component.

kinematic viscosity, such that density and dynamic viscosity do not appear. Thus, by matching the initial kinematics (root-mean-square velocity) and the corresponding dissipation (kinematic viscosity) in the two fluids, the turbulence decays at the same rate in the two fluids, even though there is an initial gradient in the kinetic energy (per unit volume). Since, the mean kinetic energy per unit mass is the same in each fluid, anisotropy initially lies in the density gradient only. Thus, anisotropy observed at later times can be attributed to this gradient, such that the effect of large-scale density differences on the turbulence can be considered, independently from any other contribution. As the flow evolves, mixing occurs between the heavy and light fluids. We explore how the mixing region grows for different density ratios and Reynolds numbers and examine both the large- and small-scale dynamics. From this study, we can make the following key conclusions.

(i) As the initial random field evolves to a turbulent state, energy gets transferred to higher wavenumbers. Over approximately the first two to four eddy turnover times, the dynamics exhibit little dependence on the density ratio. After this initial transient and once decay becomes important, the distribution of energy reverses as the small scales dissipate faster.

(ii) After the initial transient, the mixing region grows self-similarly through a process that can be described by turbulence diffusion. Several theoretical arguments are proposed to describe how the mixing region width scales with

time, in agreement with the simulations results and past work. For higher density ratios, it takes a longer time to achieve self-similar growth. The observed time exponent for the growth of the mixing region in this study is close to those reported in studies of turbulent mixing following the Richtmyer–Meshkov instability after reshock (Tritschler *et al.* 2014). This observation is expected, since the turbulence produced by such flows is very similar to that in the present study.

(iii) Bubbles and spikes grow in an asymmetric fashion due to the higher momentum of heavier eddies in the mixing region. As a result, the mid-plane corresponding to $\langle Y \rangle = 0.5$ shifts toward the lighter fluid as the density ratio is increased. This observation is important in the context of the Rayleigh–Taylor instability, as the temporal evolution of turbulence statistics is often reported at the $z = 0$ plane.

(iv) While a wider mixing region is achieved at higher density ratios, the flow is found to be less molecularly mixed therein.

 (v) At the Taylor scale, the turbulence remains almost isotropic at modest density ratios ($\rho_2/\rho_1 = 1$ and 3), while it becomes clearly anisotropic at higher density ratios ($\rho_2/\rho_1 = 8$, and 12). The fact that the flow is almost isotropic at the Taylor scale for $\rho_2/\rho_1 = 3$ is particularly important in terms of Rayleigh–Taylor turbulence, as many past DNS have been performed at this density ratio (Cook & Dimotakis 2001; Cabot & Cook 2006); typically the anisotropy in the composition is also considered as one of the main sources of anisotropy in addition to gravity in these flows. The scalar field appears to remains almost isotropic up to the Corrsin scale, even for high density ratios.

(vi) Flow intermittency is investigated by measuring the skewness and kurtosis of the velocity and the scalar derivatives in different directions. The intermittency of the velocity field remains the same in different directions and takes values corresponding to grid turbulence. The scalar field is more intermittent than the velocity and exhibits larger intermittency in the direction of the scalar gradient, in agreement with past grid-turbulence experiments.

This paper constitutes the first in a series on level 2 turbulent mixing and lays the foundations for understanding how density gradients lead to anisotropy. Our next study will focus on the combined effect of a gravitational field with a density gradient, specifically in the context of Rayleigh–Taylor turbulence.

Acknowledgements

REFERENCES

ABARZHI, S. I. 2010 On fundamentals of Rayleigh–Taylor turbulent mixing. *Europhys. Lett.* **91**, 35001.

ABARZHI, S. I., GOROBETS, A. & SREENIVASAN, K. R. 2005 Rayleigh–Taylor turbulent mixing of immiscible, miscible and stratified fluids. *Phys. Fluids* **17**, 081705.

ANAND, M. S. & POPE, S. B. 1983 Diffusion behind a line source in grid turbulence. *Turbulent Shear Flows* **4**, 46–61.

ANTONIA, R. A., LEE, S. K., DJENIDI, L., LAVOIE, P. & DANAILA, L. 2013 Invariants for slightly heated decaying grid turbulence. *J. Fluid Mech.* **727**, 379–406.

BATCHELOR, G. K. & PROUDMAN, I. 1956 The large-scale structure of homogeneous turbulence. *Phil. Trans. R. Soc. Lond.* A **248**, 369–405.

BHAGATWALA, A. & LELE, S. K. 2011 Interaction of a Taylor blast wave with isotropic turbulence. *Phys. Fluids* **23**, 035103.

BHAGATWALA, A. & LELE, S. K. 2012 Interaction of a converging spherical shock wave with isotropic turbulence. *Phys. Fluids* **24**, 085102.

BLAISDELL, G. A., SPYROPOULOS, E. T. & QIN, J. H. 1996 The effect of the formulation of nonlinear terms on aliasing errors in spectral methods. *Appl. Numer. Maths* **21**, 207–219.

BROUILLETTE, M. 2002 The Richtmyer–Meshkov instability. *Annu. Rev. Fluid Mech.* **34**, 445–468.

CABOT, W. H. & COOK, A. W. 2006 Reynolds number effects on Rayleigh–Taylor instability with possible implications for type-Ia supernovae. *Nat. Phys.* **2**, 562–568.

CABOT, W. & ZHOU, Y. 2013 Statistical measurements of scaling and anisotropy of turbulent flows induced by Rayleigh–Taylor instability. *Phys. Fluids* **25**, 015107.

CHANDRASEKHAR, S. 1961 *Hydrodynamic and Hydromagnetic Stability*. Oxford University Press.

COMTE-BELLOT, G. & CORRSIN, S. 1966 Use of a contraction to improve isotropy of grid-generated turbulence. *J. Fluid Mech.* **25** (4), 657–682.

COOK, A. W. & DIMOTAKIS, P. E. 2001 Transition stages of Rayleigh–Taylor instability between miscible fluids. *J. Fluid Mech.* **443**, 69–99.

CORRSIN, S. 1951 On the spectrum os isotropic temperature fluctuations in an isotropic turbulence. *J. Appl. Phys.* **22** (4), 469–473.

DANCKWERTS, P. V. 1952 The definition and measurement of some characteristics of mixtures. *Appl. Sci. Res.* **3** (4), 279–296.

DANCKWERTS, P. V. 1958 The effect of incomplete mixing on homogeneous reactions. *Chem. Engng Sci.* **8** (1), 93–102.

DIMONTE, G., YOUNGS, D. L., DIMITS, A., WEBER, S., MARINAK, M., WUNSCH, S., GARASI, C., ROBINSON, A., ANDREWS, M. J., RAMAPRABHU, P., CALDER, A. C., FRYXELL, B., BIELLO, J., DURSI, L., MACNEICE, P., OLSON, K., RICKER, P., ROSNER, R., TIMMES, F., TUFO, H., YOUNG, Y. N. & ZINGALE, M. 2004 A comparative study of the turbulent Rayleigh–Taylor instability using high-resolution three-dimensional numerical simulations: the Alpha-Group collaboration. *Phys. Fluids* **16** (5), 1668–1693.

DIMOTAKIS, P. E. 2000 The mixing transition in turbulent flows. *J. Fluid Mech.* **409**, 69–98.

DIMOTAKIS, P. E. 2005 Turbulent mixing. *Annu. Rev. Fluid Mech.* **37**, 329–356.

DRAKE, R. P. 2006 *High-Energy Density Physics*, 1st edn. Springer.

DUCROS, F., LAPORTE, F., SOULERES, T., GUINOT, V., MOINAT, P. & CARUELLE, B. 2000 High-order fluxes for conservative skew-symmetric-like schemes in structured meshes: application to compressible flows. *J. Comput. Phys.* **161**, 114–139.

EYINK, G. L. & ALUIE, H. 2009 Localness of energy cascade in hydrodynamic turbulence. I. Smooth coarse graining. *Phys. Fluids* **21** (11), 115107.

GEORGE, W. K. 1992 The decay of homogeneous isotropic turbulence. *Phys. Fluids* A **4** (7), 1492–1509.

GOTTLIEB, S. & SHU, C. W. 1998 Total variation diminishing Runge–Kutta schemes. *Maths Comput.* **67**, 73–85.

HILL, D. J., PANTANO, C. & PULLIN, D. I. 2006 Large-eddy simulation and multiscale modelling of a Richtmyer–Meshkov instability with reshock. *J. Fluid Mech.* **557**, 29–61.

HUQ, P. & BRITTER, R. E. 1995a Mixing due to grid-generated turbulence of a two-layer scalar profile. *J. Fluid Mech.* **285**, 17–40.

HUQ, P. & BRITTER, R. E. 1995b Turbulence evolution and mixing in a two-layer stably stratified fluid. *J. Fluid Mech.* **285**, 41–67.

JAYESH, TONG, C. N. & WARHAFT, Z. 1994 On temperature spectra in grid turbulence. *Phys. Fluids* **6** (1), 306–312.

JOHNSEN, E., LARSSON, J., BHAGATWALA, A. V., CABOT, W. H., MOIN, P., OLSON, B. J., RAWAT, P. S., SHANKAR, S. K., SJOGREEN, B., YEE, H. C., ZHONG, X. & LELE, S. K. 2010 Assessment of high-resolution methods for numerical simulations of compressible turbulence with shock waves. *J. Comput. Phys.* **229**, 1213–1237.

JOSEPH, D. D. 1990 Fluid dynamics of two miscible liquids with diffusion and gradient stresses. *Eur. J. Mech. (B/Fluids)* **9** (6), 565–596.

KIFONIDIS, K., PLEWA, T., SCHECK, L., JANKA, H. T. & MULLER, E. 2006 Non-spherical core collapse supernovae – II. The late-time evolution of globally anisotropic neutrino-driven explosions and their implications for SN 1987 A. *Astron. Astrophys.* **453**, 661–678.

KOLMOGOROV, A. N. 1941 The local structure of turbulence in incompressible viscous fluid for very large Reynolds numbers. *Dokl. Akad. Nauk SSSR* **30**, 301.

KROGSTAD, P. A. & DAVIDSON, P. A. 2010 Is grid turbulence Saffman turbulence? *J. Fluid Mech.* **642**, 373–394.

LAMRIBEN, C., CORTET, P. & MOISY, F. 2011 Direct measurements of anisotropic energy transfers in a rotating turbulence experiment. *Phys. Rev. Lett.* **107** (2), 024503.

LARSSON, J. & LELE, S. K. 2009 Direct numerical simulation of canonical shock/turbulence interaction. *Phys. Fluids* **21**, 126101.

LAWRIE, A. G. W. & DALZIEL, S. B. 2011 Turbulent diffusion in tall tubes. I. Models for Rayleigh–Taylor instability. *Phys. Fluids* **23**, 085109.

LAYZER, D. 1955 On the instability of superposed fluids in a gravitational field. *Astrophys. J.* **122**, 1–12.

LEE, S., LELE, S. K. & MOIN, P. 1991 Eddy shocklets in decaying compressible turbulence. *Phys. Fluids* **3**, 657–664.

LINDEN, P. F. 1980 Mixing across a density interface produced by grid turbulence. *J. Fluid Mech.* **100**, 691–703.

LINDL, J. 1995 Development of the indirect-drive approach to inertial confinement fusion and the target physics basis for ignition and gain. *Phys. Plasmas* **2**, 3933–4024.

LIVESCU, D., JABERI, F. A. & MADNIA, C. K. 2000 Passive-scalar wake behind a line source in grid turbulence. *J. Fluid Mech.* **416**, 117–149.

LIVESCU, D. & RISTORCELLI, J. R. 2007 Buoyancy-driven variable-density turbulence. *J. Fluid Mech.* **591**, 43–71.

LIVESCU, D. & RISTORCELLI, J. R. 2008 Variable-density mixing in buoyancy-driven turbulence. *J. Fluid Mech.* **605**, 145–180.

LIVESCU, D., RISTORCELLI, J. R., PETERSEN, M. R. & GORE, R. A. 2010 New phenomena in variable-density Rayleigh–Taylor turbulence. *Phys. Scr. T* **2010** (142), 014015.

MONIN, A. S. & YAGLOM, A. M. 1975 *Statistical Fluid Mechanics*. MIT Press.

MOVAHED, P. 2014 High-fidelity numerical simulations of compressible turbulence and mixing generated by hydrodynamic instabilities. PhD thesis, University of Michigan.

MOVAHED, P. & JOHNSEN, E. 2011 Numerical simulations of the Richtmyer–Meshkov instability with reshock. *AIAA Paper* 2011-3680.

MOVAHED, P. & JOHNSEN, E. 2013a A solution-adaptive method for efficient compressible multifluid simulations, with application to the Richtmyer–Meshkov instability. *J. Comput. Phys.* **239**, 166–186.

MOVAHED, P. & JOHNSEN, E. 2013b Turbulence diffusion effects at material interfaces, with application to the Rayleigh–Taylor instability. *AIAA Paper* 2013-3121.

MUESCHKE, N. J. & SCHILLING, O. 2009 Investigation of Rayleigh–Taylor turbulence and mixing using direct numerical simulation with experimentally measured initial conditions. I. Comparison to experimental data. *Phys. Fluids* **21**, 014106.

MYDLARSKI, L. & WARHAFT, Z. 1998 Passive scalar statistics in high-Peclet-number grid turbulence. *J. Fluid Mech.* **358**, 135–175.

NASO, A. & PUMIR, A. 2005 Scale dependence of the coarse-grained velocity derivative tensor structure in turbulence. *Phys. Rev. E* **72** (5), 056318.

NASO, A., PUMIR, A. & CHERTKOV, M. 2006 Scale dependence of the coarse-grained velocity derivative tensor: influence of large-scale shear on small-scale turbulence. *J. Turbul.* **7**, 1–11.

OBUKHOV, A. M. 1949 Structure of the temperature field in turbulent flows. *Izv. Akad. Nauk SSSR Geogr. Geofiz.* **13**, 1–58.

PIROZZOLI, S. 2011 Numerical methods for high-speed flows. *Annu. Rev. Fluid Mech.* **43**, 163–194.

POPE, S. 2000 *Turbulent Flows*. Cambridge University Press.

POUJADE, O. 2006 Rayleigh–Taylor turbulence is nothing like Kolmogorov turbulence in the self-similar regime. *Phys. Rev. Lett.* **97**, 185002.

RAMAPRABHU, P., KARKHANIS, V. & LAWRIE, A. G. W. 2013 The Rayleigh–Taylor Instability driven by an accel–decel–accel profile. *Phys. Fluids* **25** (11), 115104.

REID, R. C., PRAUSNITZ, J. M. & POLING, B. E. 1987 *The Properties of Gases and Liquids*, 4th edn. McGraw-Hill.

RISTORCELLI, J. R. & BLAISDELL, G. A. 1997 Consistent initial conditions for the DNS of compressible turbulence. *Phys. Fluids* **9**, 4–6.

RISTORCELLI, J. R. & CLARK, T. T. 2004 Rayleigh–Taylor turbulence: self-similar analysis and direct numerical simulations. *J. Fluid Mech.* **507**, 213–253.

ROGERS, M. M. & MOSER, R. D. 1992 The three-dimensional evolution of a plane mixing layer: the Kelvin–Helmholtz rollup. *J. Fluid Mech.* **243**, 183–226.

SAFFMAN, P. J. 1967 The large-scale structure of homogeneous turbulence. *J. Fluid Mech.* **27**, 581–593.

SAMTANEY, R., PULLIN, D. I. & KOSOVIC, B. 2001 Direct numerical simulation of decaying compressible turbulence and shocklet statistics. *Phys. Fluids* **13** (5), 1415–1430.

SAWFORD, B. 2001 Turbulent relative dispersion. *Annu. Rev. Fluid Mech.* **33**, 289–317.

SHARP, D. H. 1984 An overview of Rayleigh–Taylor instability. *Physica* D **12**, 3–18.

SOULARD, O. & GRIFFOND, J. 2012 Inertial-range anisotropy in Rayleigh–Taylor turbulence. *Phys. Fluids* **24**, 025101.

SREENIVASAN, K. R. & ANTONIA, R. A. 1997 The phenomenology of small-scale turbulence. *Annu. Rev. Fluid Mech.* **29**, 435–472.

STAPOUNTZIS, H., SAWFORD, B. L., HUNT, J. C. R. & BRITTER, R. E. 1986 Structure of the temperature-field downwind of a line source in grid turbulence. *J. Fluid Mech.* **165**, 401–424.

TAO, B., KATZ, J. & MENEVEAU, C. 2002 Statistical geometry of subgrid-scale stresses determined from holographic particle image velocimetry measurements. *J. Fluid Mech.* **457**, 35–78.

THOMAS, V. A. & KARES, R. J. 2012 Drive asymmetry and the origin of turbulence in an ICF implosion. *Phys. Rev. Lett.* **109**, 075004.

THOMPSON, K. W. 1987 Time-dependent boundary-conditions for hyperbolic systems. *J. Comput. Phys.* **68**, 1–24.

THORNBER, B., DRIKAKIS, D., YOUNGS, D. L. & WILLIAMS, R. J. R. 2011 Growth of a Richtmyer–Meshkov turbulent layer after reshock. *Phys. Fluids* **23**, 095107.

TONG, C. N. & WARHAFT, Z. 1994 On passive scalar derivative statistics in grid turbulence. *Phys. Fluids* **6** (6), 2165–2176.

TORDELLA, D. & IOVIENO, M. 2006 Numerical experiments on the intermediate asymptotics of shear-free turbulent transport and diffusion. *J. Fluid Mech.* **549**, 429–441.

TORDELLA, D. & IOVIENO, M. 2011 Small-scale anisotropy in turbulent shearless mixing. *Phys. Rev. Lett.* **107**, 194501.

TORDELLA, D. & IOVIENO, M. 2012 Decaying turbulence: What happens when the correlation length varies spatially in two adjacent zones. *Physica* D **241**, 178–185.

TORDELLA, D., IOVIENO, M. & BAILEY, P. R. 2008 Sufficient condition for Gaussian departure in turbulence. *Phys. Rev.* E **77**, 016309.

TRITSCHLER, V. K., OLSON, B. J., LELE, S. K., HICKEL, S., HU, X. Y. & ADAMS, N. A. 2014 On the Richtmyer–Meshkov instability evolving from a deterministic multimode planar interface. *J. Fluid Mech.* **755**, 429–462.

TURNER, J. S. 1968 The influence of molecular diffusivity on turbulent entrainment across a density interface. *J. Fluid Mech.* **33**, 639–656.

WARHAFT, Z. 1984 The interference of thermal fields from line sources in grid turbulence. *J. Fluid Mech.* **144**, 363–387.

WARHAFT, Z. 2000 Passive scalars in turbulent flows. *Annu. Rev. Fluid Mech.* **32**, 203–240.

WATANABE, T. & GOTOH, T. 2006 Intermittency in passive scalar turbulence under the uniform mean scalar gradient. *Phys. Fluids* **18**, 058105.

WATANABE, T. & GOTOH, T. 2007 Inertial-range intermittency and accuracy of direct numerical simulation for turbulence and passive scalar turbulence. *J. Fluid Mech.* **590**, 117–146.